Article
journal of Studies of Earth's Deep Interior
doi:10.46298/jsedi.17790

Geodynamo simulations spanning millennia in the physical conditions of Earth's core

Julien Aubert * [1]

[1]Université Paris Cité, Institut de physique du globe de Paris, CNRS, F-75005 Paris, France

Abstract A geodynamo simulation is presented where the Earth's core density, rotation rate, convective power and electrical conductivity are matched, while viscous losses are maintained minor in the force balance and power budget. Improving over earlier preliminary calculations, the simulation is integrated over near 1700 years in physical time, and realistically renders the time scale range between interannual hydromagnetic waves and secular convective motions. The solution has been obtained by gradually approaching these conditions along a path in model parameter space. A quasi-geostrophic, magneto-Archimedes-Coriolis (QG-MAC) force balance is confirmed, with the characteristic length scale of the system remaining near the planetary scale. Without the need for extrapolation, the morphology, variations and dynamics of the velocity, convective density anomaly and magnetic fields are in excellent quantitative agreement with geomagnetic and geodetic observations supplied over the past centuries by navigation, observatories and satellites. In particular, the simulation reveals the contribution of interdecadal magneto-Coriolis waves to geomagnetic variations in the vicinity of 60-yr periods. This direct validation of the convective geodynamo paradigm additionally offers a quantitative and first principle-based physical link between the observable signals and deep Earth geodynamic parameters. The model confirms that a convective power (or ohmic dissipation) level near 3 TW is needed to account for the observed geomagnetic variations, and that the top of the core should be convectively neutral or unstable. Explaining the core-originated interannual to decadal variations of the length of day through electromagnetic core-mantle coupling requires a lower mantle conductance on the order of 10^9 S. It may also become possible to constrain the outer core electrical conductivity from the observed patterns of interannual magneto-Coriolis waves. Finally, the simulation can be considered a reliable source of prior information for solving geomagnetic inverse and prediction problems.

Handling Editor:
Stéphane Labrosse
Received:
March 23, 2026
Revised:
May 4, 2026
Accepted:
May 4, 2026
Published:
May 5, 2026

1 Introduction

The goal of geodynamo studies is to understand and predict the physics of the convectively-driven, rotating fluid dynamo that generates Earth's magnetic field within the electrically conducting fluid core of the planet. The physical conditions in which this system operates may first be defined by a typical dimension $D = 2260$ km (the outer core thickness), mean core density $\rho = 1.1 \times 10^4$ kg/m^3 (Ahrens, 1995), and planetary rotation rate $\Omega = 7.29 \times 10^{-5}$ s^{-1}. With these at hand, the specification of a power input (or dissipation rate) $P \approx 3$ TW (e.g. Labrosse, 2015; Nimmo, 2015; Frost et al., 2022; Aubert, 2023) leads to a typical flow velocity $U = (P/\rho\Omega D^3)^{1/2} \approx 5 \times 10^{-4}$ m.s^{-1} (e.g. Aubert et al., 2017). The dominance of the Coriolis force on this flow may be measured by the Rossby number $Ro = U/\Omega D \approx 3 \times 10^{-6}$. The hydrodynamic turbulence is characterised by the Reynolds number $Re = UD/\nu \approx 10^9$, with the fluid viscosity $\nu \approx 10^{-6}$ m^2.s^{-1} (de Wijs et al., 1998). Earth's core conditions are therefore ones of rapid rotation, strong power input, and low viscous dissipation, and naturally lead to high levels of flow turbulence, the details of which have remained out of reach of numerical simulations, and will remain so for the foreseeable future.

The past three decades have nevertheless seen the development of a constant stream of first-principle based simulations with increasing realism. To summarise a few key steps, the discipline took off with the obtention of self-sustained, Earth-like magnetic fields with dipoles that can reverse polarity (Glatzmaier and Roberts, 1995; Kuang and Bloxham, 1997; Kageyama et al., 1995). This was a remarkable success given the strong approximations that were used at the time. Fluid flow was indeed simulated only at large scales and the turbulence was damped with the help of hyperdiffusivity, or by partially or totally dropping inertial terms in the equation for fluid motion. A standard formulation later dropped some of these approximations at the expense of more modest computing parameters (see Christensen et al., 2001), and the associated benchmarks promoted a significant increase in the size of the research community dedicated to the problem. The standard formulation also enabled a deeper understanding of the conditions for magnetic field generation and equilibration (Olson et al., 1999). Systematic explorations of the parameter space could then be performed (e.g. Kutzner and Christensen, 2002; Christensen and Aubert, 2006; Christensen et al., 2010; Soderlund et al., 2015; Yadav et al., 2016; Schwaiger et al., 2019; Menu et al., 2020; Teed and Dormy, 2025), in order to map regions where the solution would present Earth-like characteristics, key dynamical regimes as well as regime transitions. Since this parameter space remained very remote from Earth's core conditions, scaling laws were also formulated (Starchenko and Jones,

*Corresponding author: aubert@ipgp.fr

2002; Christensen and Aubert, 2006; Davidson, 2013) to extrapolate the model output to these conditions. The scaling laws guided further pointwise samplings of the parameter space at more computationally demanding conditions (e.g. Takahashi et al., 2005; Kageyama et al., 2008; Sakuraba and Roberts, 2009; Miyagoshi et al., 2010; Schaeffer et al., 2017; Sheyko et al., 2018). They also promoted the theoretical design of paths connecting the parameter space regions where tractable models had been found to the region where Earth's core resides (Aubert et al., 2017), while preserving those aspects of the solutions that had been successfully compared to observations.

Though rotating hydrodynamic turbulence is a topic of interest in itself and best approached by laboratory experiments (e.g. Aurnou et al., 2015; Nataf and Schaeffer, 2015; Le Bars and Lemasquerier, 2026), its accurate small-scale description may be only of secondary importance on the way towards simulating the geodynamo in the physical conditions of Earth's core. The magnetic to kinetic energy ratio of the core is about $B^2/\rho\mu U^2 \approx 5000$, using the above values of U, ρ, the permeability $\mu = 4\pi \times 10^{-7}$ H.m^{-1} and typical magnetic field intensity $B = 4$ mT (Gillet et al., 2010). Most of the energy is therefore contained in the magnetic field itself. The route taken by the system from energy input to dissipation does rather involve a much less intense magnetic nonlinearity, and ultimately ohmic losses at fairly large scales (typically a few tenths of kilometers, e.g. Christensen and Tilgner, 2004), because the magnetic diffusivity $\eta = O(1\ \mathrm{m}^2.\mathrm{s}^{-1})$ (e.g. Berrada and Secco, 2021) is much larger than the fluid viscosity ν. Only a small fraction of the energy is expected to cascade further down towards the much smaller scales of viscous dissipation. It is then possible to preserve the large-scale structure and dynamics of fully-resolved simulations when enhancing the small-scale values for ν, provided that dissipation remains predominantly of ohmic nature (Aubert, 2019). This rationalises the success of early geodynamo models, and incidentally also matches the intuition of Glatzmaier (2002), when he considered as a 'grand challenge' a simulation with ρ, Ω, P, η set to their Earth values and ν larger than its molecular value but still as small as possible (and no larger than η), on the basis of turbulent diffusivity arguments (see also Gubbins, 2001). Introducing such large-scale approximations has led to simulations that could approach close to Earth's core conditions thanks to tractable spatial resolution, but still with increasing demands on temporal resolution (Aubert and Gillet, 2021). The computation indeed remains a challenge because the low target value of the magnetic Ekman number $E_\eta = \eta/\Omega D^2 = O(10^{-9})$ requires to resolve a planetary rotation period that is extremely short respectively to the magnetic energy dissipation time scale. Some recent simulations have finally reached Earth's core physical conditions over short integration times of a few decades to a century in physical time (Aubert, 2023; Aubert, 2025).

This study introduces the first geodynamo simulations reaching Earth's core conditions (correct values for ρ, Ω, P, η, and $\nu \ll \eta$ at large scales but enhanced at small scales) over durations ranging from several centuries up to millennia in physical time. The simulation therefore renders hydromagnetic waves occurring at interannual periods as well as the convective circulation responsible for secular geomagnetic variations. This work is intended to serve several purposes. First, we wish to confirm that over a significant number of overturn times and without the need for any extrapolation, the paradigm of a convective geodynamo is successful at predicting most observations acquired in the past centuries with magnetic observatories, navigation data and satellites. Second, in the new simulation all the important physical time scales are now correctly placed within the interannual to secular time scale range. This enables an accurate comparison of the model output with geomagnetic variations in this range, and provides further insight into their origin and cross-timescale interplay. Third, here we vary some key physical properties of the model, in an attempt to provide geomagnetic constraints on their Earth values, as well as further information on the present thermal state of Earth's core. Finally, the new models are intended to provide robust prior information for inverse- and data assimilation-based problems, for instance for determining the fluid flow beneath the core surface from geomagnetic data (e.g. Gillet et al., 2022; Istas et al., 2023; Gillet et al., 2024), and for building mathematical models of the geomagnetic field with high temporal resolution (Claveau et al., 2025; Kloss et al., 2026).

This manuscript is laid out as follows: section 2 describes the numerical model, the results are presented in section 3 and discussed in section 4.

2 Methods

2.1 Model description

We solve for Boussinesq convection and magnetic induction within a spherical shell of thickness $D = r_o - r_i$, aspect ratio $r_i/r_o = 0.35$ representing Earth's outer core. The gravity $\mathbf{g} = -g_o r/r_o \mathbf{e}_r$ is radial. The shell is rotating with angular velocity $\mathbf{\Omega} = \Omega \mathbf{e}_z$ and contains an incompressible Newtonian fluid of uniform density ρ, viscosity ν, thermo-chemical diffusivity κ and electrical conductivity σ (the magnetic diffusivity is $\eta = 1/\mu\sigma$). We choose a spherical coordinate system (r, θ, φ) with unit vectors $\mathbf{e}_r, \mathbf{e}_\theta, \mathbf{e}_\varphi$ associated to the cylindrical system (s, z, φ) of unit vectors $\mathbf{e}_s, \mathbf{e}_z, \mathbf{e}_\varphi$. Our unknowns are the velocity field $\mathbf{u}$, magnetic field $\mathbf{B}$ and codensity (opposite of density anomaly) field C. In the rotating frame, the governing equations are

$$\rho\left(\frac{\partial \mathbf{u}}{\partial t} + \mathbf{u}\cdot\boldsymbol{\nabla}\mathbf{u}\right) + 2\rho\Omega\mathbf{e}_z \times \mathbf{u} + \boldsymbol{\nabla}\Pi = g_o \frac{r}{r_o} C\mathbf{e}_\mathbf{r} + \frac{1}{\mu}(\boldsymbol{\nabla}\times\mathbf{B})\times\mathbf{B} + \rho\nu\boldsymbol{\nabla}^2\mathbf{u}, \tag{1a}$$

$$\frac{\partial \mathbf{B}}{\partial t} = \boldsymbol{\nabla}\times(\mathbf{u}\times\mathbf{B}) + \eta\boldsymbol{\nabla}^2\mathbf{B}, \tag{1b}$$

$$\frac{\partial C}{\partial t} + \mathbf{u}\cdot\boldsymbol{\nabla}C = \kappa\nabla^2 C + S_C, \tag{1c}$$

$$\boldsymbol{\nabla}\cdot\mathbf{u} = 0, \tag{1d}$$

$$\boldsymbol{\nabla}\cdot\mathbf{B} = 0. \tag{1e}$$

Here Π is the pressure field. The mechanical boundary conditions are of stress-free and non-penetrating type at both boundaries (see Aubert et al., 2017, for a justification of stress-free boundaries for modelling the geodynamo). The shell is electromagnetically coupled at $r = r_i$ with a solid inner core of same density and conductivity, featuring an axial differential rotation Ω_{IC} in the rotating frame. At $r = r_o$, the shell is also coupled to another shell between radii r_o and

$r_E = 1.83 r_o$ (Earth's radius) representing the mantle, presenting a thin conducting layer of thickness Δ and conductivity σ_M at its base. The mantle also presents an axial differential rotation Ω_M in the rotating frame.

The models use the co-density approximation which merges thermal and chemical buoyancy into a single field C with a single diffusivity κ. Convection is driven by imposed homogeneous mass anomaly fluxes $F_i = -4\pi\kappa r_i^2 \partial C/\partial r(r_i)$ and $F_o = -4\pi\kappa r_o^2 \partial C/\partial r(r_o)$ at both boundaries, meant to respectively represent the buoyancy arising from inner core crystallisation and from a superadiabatic core-mantle boundary heat flow. The total mass anomaly flux is $F = F_i + F_o$ and the inner core-originated fraction is noted $f_i = F_i/F$. Mass is preserved through the specification of a sink term $S_C = (F_o - F_i)/V = 3(1-2f_i)F/4\pi(r_o^3 - r_i^3)$, where V is the shell volume. At each boundary, heterogeneous mass anomaly fluxes can be superimposed with peak-to-peak amplitudes Δf_i, Δf_o and patterns as in Aubert et al. (2013). This is used in one of our models (case C, see section 2.4) to mimic the effects of a longitudinally hemispheric inner core growth pattern at $r = r_i$, and of thermal control from a laterally heterogeneous mantle at $r = r_o$.

The inner core and mantle are furthermore gravitationally coupled together using the model of Buffett (1996); Buffett (1997). A misalignment angle Φ between the inner core and mantle is introduced, and the gravitational torque exerted on the inner core is then $\Gamma_G = -\Gamma\Phi$, where Γ is a coupling constant. The misalignment angle can relax because of the finite viscosity of the inner core, following

$$\frac{\mathrm{d}\Phi}{\mathrm{d}t} + \frac{\Phi}{\tau_{IC}} = \Omega_{IC} - \Omega_M, \tag{2}$$

where τ_{IC} is the viscous relaxation time of the inner core. Our models either use a finite value of τ_{IC}, or the instantaneous relaxation limit $\tau_{IC} \to 0$ where the gravitational torque felt by the inner core simply becomes $\Gamma_G = -\Gamma\tau_{IC}(\Omega_{IC} - \Omega_M)$. In this case neither Γ nor τ_{IC} have a physical meaning in isolation and only their product has one.

We solve for the coupled rotational dynamics of the inner core-outer core-mantle system. The evolution equations for the inner core and mantle axial differential rotations are

$$I_{IC}\frac{\mathrm{d}\Omega_{IC}}{\mathrm{d}t} = \Gamma_{M,I} + \Gamma_G, \tag{3a}$$

$$I_M\frac{\mathrm{d}\Omega_M}{\mathrm{d}t} = \Gamma_{M,M} - \Gamma_G, \tag{3b}$$

where I_{IC}, I_M are the inner core and mantle moments of inertia, $\Gamma_{M,I}$ and $\Gamma_{M,M}$ are the electromagnetic torques felt by the inner core and mantle. We recall that (Rochester, 1962)

$$\Gamma_{M,I} = \frac{r_i}{\mu}\iint_{r=r_i} B_r B_\varphi \sin\theta \,\mathrm{d}S, \tag{4a}$$

$$\Gamma_{M,M} = -\frac{r_o}{\mu}\iint_{r=r_o} B_r B_\varphi \sin\theta \,\mathrm{d}S, \tag{4b}$$

where $B_r = \mathbf{B}\cdot\mathbf{e}_r$ and $B_\varphi = \mathbf{B}\cdot\mathbf{e}_\varphi$. The angular momentum of the coupled system is preserved at each instant.

2.2 Dimensionless input parameters and parameter space paths

Though this becomes optional once Earth's core conditions are reached, for consistency with previous work the system of equations (1) is solved in a dimensionless form, where a number of fundamental input parameters appear. A useful scheme is to adimension length with D, time with Ω^{-1}, magnetic field with $\sqrt{\rho\mu\Omega\eta}$ and density anomaly with $F/4\pi\Omega D^3$. The resulting dimensionless equations can be found e.g. in Aubert et al. (2017). The classical dimensionless input parameters are the flux-based Rayleigh, magnetic Ekman, Prandtl and magnetic Prandtl numbers

$$Ra_F = \frac{g_o F}{4\pi\rho\Omega^3 D^4}, \tag{5a}$$

$$E_\eta = \frac{\eta}{\Omega D^2}, \tag{5b}$$

$$Pr = \frac{\nu}{\kappa}, \tag{5c}$$

$$Pm = \frac{\nu}{\eta}. \tag{5d}$$

Adding to these are three additional parameters describing the couplings and rotational dynamics, the mantle conductance ratio $\Sigma = \Delta\sigma_M/D\sigma$, the dimensionless inner core viscous relaxation time $\tau_{IC}\Omega$ and the dimensionless gravitational coupling constant $\xi = \Gamma\tau_{IC}/\rho D^5\Omega$. See the Supplementary Spreadsheet (link in the data availability statement) for the dimensionless parameter values used in this study.

It is useful to approach Earth's core physical conditions by considering suites of models with increasingly realistic parameters. These follow parameter space paths along which the leading-order force balance and level of magnetic induction are preserved (Aubert et al., 2017). A path parameter ϵ is introduced and governs the other dimensionless parameter along a given path, according to the following rules:

$$Ra_F = \epsilon Ra_F(0), E_\eta = \sqrt{\epsilon}E_\eta(0), Pm = \sqrt{\epsilon}Pm(0), \tag{6}$$

where quantities with label '(0)' refer to the 'start of path' values at $\epsilon = 1$ located in a numerically more tractable region of the parameter space. The 'end of path', corresponding to core conditions and where all the cases presented here are located, is conventionally set at $\epsilon = 10^{-7}$. Note that the path is designed such that E_η and Ra_F have Earth-like values at the end, but Pm does not need to terminate at its Earth value as long as it becomes much smaller than unity i.e. as long as a low-viscosity limit $\nu \ll \eta$ is reached, consistently with the definition of core conditions in section 1 (see also Aubert et al., 2017). Within our set of models, the parameters for case C are chosen so that this case terminates the exploration of a path started in Aubert et al. (2017); Aubert (2019); Aubert and Gillet (2021). The main parameters of this path are $Ra_F(0) = 2.7\times10^{-5}$, $E_\eta(0) = 1.2\times10^{-5}$, $Pm(0) = 2.5$, with Pr set to unity throughout this path (there is no theoretically set rule for this parameter). We will also compare case U to its start of path equivalent U0% following the rules in Eq. (6) together with $Pr = \sqrt{\epsilon}Pr(0)$, $\xi = \sqrt{\epsilon}\,\xi(0)$ and $\Sigma = \Sigma(0)$. The parameters of this second path are therefore $Ra_F(0) = 2.7\times10^{-5}$, $E_\eta(0) = 6.98\times10^{-6}$, $Pm(0) = 4.3$, $Pr(0) = 5$, $\Sigma(0) = 10^{-4}$ and $\xi(0) = 2.1$.

2.3 Model outputs

In each of our cases, we monitor the root-mean squared velocity U and magnetic field B within the shell. This defines the overturn and Alfvén time scales $\tau_U = D/U$ and $\tau_A =$

$D\sqrt{\rho\mu}/B$. These two time scales are classically intercompared via the Alfvén number $A = \tau_A/\tau_U$. They are furthermore compared to the planetary rotation time scale $\tau_\Omega = 1/\Omega$ via the Rossby number $Ro = \tau_\Omega/\tau_U$ and the Lehnert number $\lambda = \tau_\Omega/\tau_A$. Finally, they are also compared to the magnetic diffusion time $\tau_\eta = D^2/\eta$ via the magnetic Reynolds number $Rm = \tau_\eta/\tau_U$ and the Lundquist number $S = \tau_\eta/\tau_A$. We also report on the convective power

$$P = \left\langle \int_V g_o \frac{r}{r_o} C\, \mathbf{u}\cdot\mathbf{e_r}\, \mathrm{d}V \right\rangle, \tag{7}$$

where the angle brackets denote a time average, as well as its density $p = P/V$. We finally report on the following outputs defined in Aubert et al. (2017): the fraction $f_{\rm ohm}$ of P that is dissipated in ohmic losses, the characteristic length scale $d_{\rm min}$ for ohmic dissipation

$$d_{\rm min} = \left(\int_V \left\langle \mathbf{B}^2 \right\rangle \mathrm{d}V \right)^{1/2} \cdot \left(\int_V \left\langle (\nabla\times\mathbf{B})^2 \right\rangle \mathrm{d}V \right)^{-1/2}, \tag{8}$$

and the level $\mathcal{T}$ of enforcement of the Taylor constraint (Taylor, 1963) along axial fluid cylinders. To compute this, we first evaluate the integrals

$$\mathcal{T}(s) = \frac{\displaystyle\int_{z_-}^{z_+} \mathbf{e}_\varphi \cdot \overline{(\nabla\times\mathbf{B})\times\mathbf{B}}\, \mathrm{d}z}{\displaystyle\int_{z_-}^{z_+} \left| \mathbf{e}_\varphi \cdot \overline{(\nabla\times\mathbf{B})\times\mathbf{B}} \right| \mathrm{d}z}. \tag{9}$$

Here the overbar represents an azimuthal average, and the vertical integrals are taken between the z-coordinates $z_{-,+}$ at which the axial cylinder of radius s intersects the spherical shell boundaries. To obtain $\mathcal{T}$, we take the time- and cylindrical radius average of $\mathcal{T}(s)$. See again the Supplementary Spreadsheet for the values of these parameters in our set of model cases.

The morphology of the output magnetic field at the model surface is characterised by the rating χ^2 introduced by Christensen et al. (2010). The typical time scale $\tau^1_{\rm SV}$ of magnetic variations is obtained by computing the time-averaged spectra $\left\langle \mathbf{B}^2(\ell) \right\rangle$ and $\left\langle \dot{\mathbf{B}}^2(\ell) \right\rangle$ of the magnetic field and its temporal variations at any altitude above the model surface, and then fitting a functional form $\tau^1_{\rm SV}/\ell$ to $\tau_{\rm SV}(\ell) = \sqrt{\left\langle \mathbf{B}^2(\ell) \right\rangle / \left\langle \dot{\mathbf{B}}^2(\ell) \right\rangle}$ between degrees $\ell = 2$ and $\ell = 13$. Similarly, the typical time scale $\tau^0_{\rm SA}$ for magnetic acceleration is obtained by computing the acceleration spectrum $\left\langle \ddot{\mathbf{B}}^2(\ell) \right\rangle$ and taking the mean of $\tau_{\rm SA}(\ell) = \sqrt{\left\langle \dot{\mathbf{B}}^2(\ell) \right\rangle / \left\langle \ddot{\mathbf{B}}^2(\ell) \right\rangle}$ between degrees $\ell = 1$ and $\ell = 13$.

For the study of torsional waves and their reflection at the core surface, we additionally introduce the fundamental torsional wave period $T_0 = \sqrt{3} r_o \tau_A / D$, and the quality factor (see Schaeffer and Jault, 2016; Gillet et al., 2017)

$$Q = S\Sigma(Br_{\rm eq}/B), \tag{10}$$

where $Br_{\rm eq}$ is the root-mean-squared value of the radial magnetic field at the equator of the shell surface. We also introduce the Alfvén speed c_A given by the magnetic field permeating axial cylinders:

$$c_A^2(s,t) = \frac{1}{(z_+ - z_-)\rho\mu} \int_{z_-}^{z_+} \overline{(\mathbf{B}\cdot\mathbf{e}_s)^2}\, \mathrm{d}z, \tag{11}$$

with $z_{-,+}$ defined as above.

For the study of magnetic jerk events, we define the jerk energy $E_{\rm J}$ similarly to Aubert and Finlay (2019); Aubert et al. (2022), by examining the energy at Earth surface of the magnetic acceleration difference between consecutive 3-year windows. We define the variations in the length of day ΔLOD corresponding to a variation $\Delta\Omega_{\rm M}$ of the mantle rotation rate as $\Delta{\rm LOD} = -2\pi\Delta\Omega_{\rm M}/\Omega^2$.

We finally report on a scale-dependent representation of the force balance in the system, similarly to our previous studies (e.g Aubert et al., 2017; Schwaiger et al., 2019). This is obtained by computing the root-mean-squared amplitude of each force in Eq. (1a) as a function of the spherical harmonic degree ℓ. Estimates of the gradient-free (solenoidal) part of this balance can also be used (e.g. Schaeffer et al., 2017; Teed and Dormy, 2025), and produce essentially the same ordering of forces. The main difference between the two approaches is that the solenoidal force balance does not provide enough constraints to set the characteristic length scale $d_\perp$ of the dynamo, such that additional closure arguments are systematically needed in scaling theories based on this solenoidal balance (Davidson, 2013; Aubert et al., 2017). In contrast, the full force balance with gradients gives access to $d_\perp = \pi D/\ell_\perp$ from the crossing degree $\ell_\perp$ between the scale-dependent buoyancy and Lorentz forces (Schwaiger et al., 2021). This is because $d_\perp$ is in fact only limited by Lenz' law i.e. the cumulative feedback between fluid dynamics (Eq. 1a) and self-sustained magnetic field generation (Eq. 1b). The effect of this law amounts to the avoidance of regions with intense magnetic tension by flow gradients, through the conversion of this tension into a magnetic pressure gradient (Aubert, 2019). The associated structural constraints are therefore preserved into the gradient part of the force balance.

2.4 Description of model cases

Tab. 1 summarises the main set-up, dimensional input and output parameters of the cases presented here, the complete list being found in the Supplementary Spreadsheet. In all cases, we also use the Earth values $\Omega = 7.29\times10^{-5}$ s^{-1}, $g_0 = 10$ m.s^{-2} and $\rho = 1.1\times10^4$ kg.m^{-3}, $I_{\rm IC} = 5\times10^{34}$ kg.m^2 and $I_{\rm M} = 7.1\times10^{37}$ kg.m^2 (Ahrens, 1995), $\Gamma = 5\times10^{19}$ N.m (Davies et al., 2014) and $\tau_{\rm IC} = 20$ yr, or $\Gamma\tau_{\rm IC} = 10^{21}$ N.m.yr in the limit $\tau_{\rm IC} \to 0$. Consistently with the discussion in section 1, the viscous and thermochemical diffusivities ν and κ are enhanced respectively to their target molecular values, uniformly across length scales or through a scale-dependent hyperdiffusive scheme (see section 2.5). Case C corresponds to the end of path for the series of models computed in Aubert et al. (2017); Aubert and Gillet (2021). It respects the set-up of these cases, with low electrical conductivity, laterally heterogeneous mass anomaly flux imposed at boundaries, viscous and thermochemical hyperdiffusion, and neutral buoyancy at the outer boundary ($f_i = 1$) representative of an exactly adiabatic core heat flow. Case C is included here for consistency with the previous formulation of the path. However, here we concentrate our analysis and numerical computation effort on new cases featuring a higher electrical conductivity $\sigma \approx 10^6$ S.m^{-1} more in line with the value proposed in the past decade by ab-initio calculations and laboratory experiments (see e.g. Pozzo et al., 2012; Gomi et al., 2013; Berrada

Table 1: (a) Set-up and main inputs, (b) outputs of the model cases. See Supplementary Spreadsheet for a complete list. 'Hdiff' lists the quantities on which hyperdiffusivity is used. 'Het' refers to the use of laterally heterogeneous boundary conditions for the convective mass anomaly flux. Earth values are taken from: (1) Davies et al. (2015); Berrada and Secco (2021), (2) de Wijs et al. (1998), (3) Tassin et al. (2021), (4) Holme (1998); Gillet et al. (2015), (5) Lister (2003); Aubert (2025), (6) Pichon et al. (2016), (7) Labrosse (2015); Nimmo (2015); Aubert (2023), (8) Holme (1998); Christensen et al. (2012); Gillet et al. (2015), (9) Gillet et al. (2010), (10) Lhuillier et al. (2011); Christensen et al. (2012), (11) Kloss et al. (2026).

(a)

Label	σ (10^6 S.m^{-1})	ν (m^2.s^{-1})	κ (m^2.s^{-1})	$\Delta\sigma_M$ (10^8 S)	Hdiff	f_i	Het	τ_{IC} (yr)
C	0.56	1.12×10^{-3}	1.12×10^{-3}	1.3	ν,κ	1	yes	0
N	1.13	1.12×10^{-3}	1.12×10^{-3}	2.5	ν,κ	1	no	0
U	0.97	1.12×10^{-3}	0.71	2.2	ν	0.75	no	0
G	0.97	1.12×10^{-3}	0.71	2.2	ν	0.75	no	20
GC	0.97	1.12×10^{-3}	0.71	21.9	ν	0.75	no	20
GL	0.97	1.12×10^{-3}	0.71	0.2	ν	0.75	no	20
Earth	0.5-1.5 (1)	10^{-6} (2)	$10^{-9}-10^{-5}$ (3)	0.3-30 (4)		0.7-1 (5)		0.02-20 (6)

(b)

Label	τ_{run} (yr)	P (TW)	U (km/yr)	B (mT)	τ_U (yr)	τ_A (yr)	τ^1_{SV} (yr)	τ^0_{SA} (yr)	χ^2
C	325	3.07	20.4	4.88	111	1.73	444	8.1	3.4
N	336	3.12	20.0	4.78	113	1.76	410	5.9	0.2
U	999	2.92	20.9	4.17	108	2.02	426	5.2	1.5
G	691	3.05	20.2	4.61	112	1.83	383	4.9	2.8
GC	134	2.99	19.9	4.42	113	1.91	430	6.7	2.9
GL	191	2.97	20.4	4.42	111	1.91	356	6.0	3.2
Earth		≈ 3(7)	$\approx 17-20$ (8)	≈ 4 (9)	110-130 (8)	≈ 2 (9)	370-470 (10)	≈ 7 (11)	

and Secco, 2021). Respectively to case C, case N removes the lateral heterogeneities and explores this higher electrical conductivity value. All other cases furthermore feature unstable buoyancy at the outer boundary ($f_i < 1$), representative of a superadiabatic core heat flow. Rather than hyperdiffusing the density anomaly field, they use an enhanced thermochemical diffusivity at all scales. Case G has been started from the end of case U, by only changing the value of the relaxation time τ_{IC} of the solid inner core. This change only influences the properties of the gravitational torque felt by the inner core at time scales shorter than τ_{IC}, such that all other outputs are continuous, differentiable, and statistically stationary when concatenating the two sequences U and G. Together, these cases span 1690 years in physical time, the longest time series to date for a model operating at these conditions. Cases GL and GC differ from G only by the value of mantle conductance.

In all models, the forcing of convection (the parameter Ra_F, or equivalently the power P which is proportional to Ra_F, e.g. Aubert et al., 2017) is set such that the output magnetic variations respect the observed time scale $\tau^1_{SV} = 370-470$ yr of geomagnetic variations (e.g. Lhuillier et al., 2011; Christensen et al., 2012). As previously shown in Aubert (2023), this tends to narrow down the range of output convective powers in the vicinity of $P \approx 3$ TW (Tab. 1). In particular, cases U and G (the longest series of this study) explore the possibility that this power level is obtained in the context of a fairly high electrical core conductivity that also corresponds to a thermal conductivity in the vicinity of $k \approx 80-90$ W.m^{-1}.K^{-1} (Pozzo et al., 2022; Ohta et al., 2025), leading to an adiabatic heat flow at the core surface in the vicinity of $Q_{ad} = 12-13$ TW (Labrosse, 2015). With multidisciplinary estimates pointing to a value $Q_{CMB} \approx 15$ TW for the total core surface heat flow, we note that core thermodynamics then indeed predicts a total dissipation or total dynamo power in the vicinity of $P \approx 3$ TW (Labrosse, 2015), underlining the internal consistency within the chosen parameter set. Consistently with the superadiabatic situation described above ($Q_{CMB} > Q_{ad}$), there is top-driven buoyancy in the system, which motivates the choice $f_i < 1$ i.e. $F_o > 0$ for the mass anomaly flux partition.

2.5 Numerical implementation

The numerical implementation rests on a spectral expansion of fields in spherical harmonics up to degree and order ℓ_{max} for the lateral directions, and of second-order finite-differences over NR grid points in the radial direction. The spherical harmonics transform library SHTns (Schaeffer, 2013) available on BitBucket is used. The time stepping scheme is semi-implicit with second-order accuracy. Cases featuring hyperdiffusivity (column Hdiff in Tab. 1) on ν and/or κ replace the native diffusivity ν (respectively κ) above degree $\ell = 30$ with an effective diffusivity $\nu_{eff} = \nu q_h^{\ell-30}$ (respectively κ_{eff}). Here q_h is a parameter governing the steepness of hyperdiffusive ramping up with harmonic degree. The physical justification and validation for this approach is given in Aubert et al. (2017); Aubert (2019). The models are integrated over a duration τ_{run} in physical time. See the Supplementary Spreadsheet for the complete list of numerical implementation parameters. The cases presented here have been obtained with a strategy of stepwise progression along parameter space paths (Aubert and Gillet, 2021; Aubert, 2023). Starting from moderate conditions, the computation is gradually advanced towards Earth's core conditions by using the path scaling laws (Aubert et al., 2017), which minimises the duration of numerical equilibration transients.

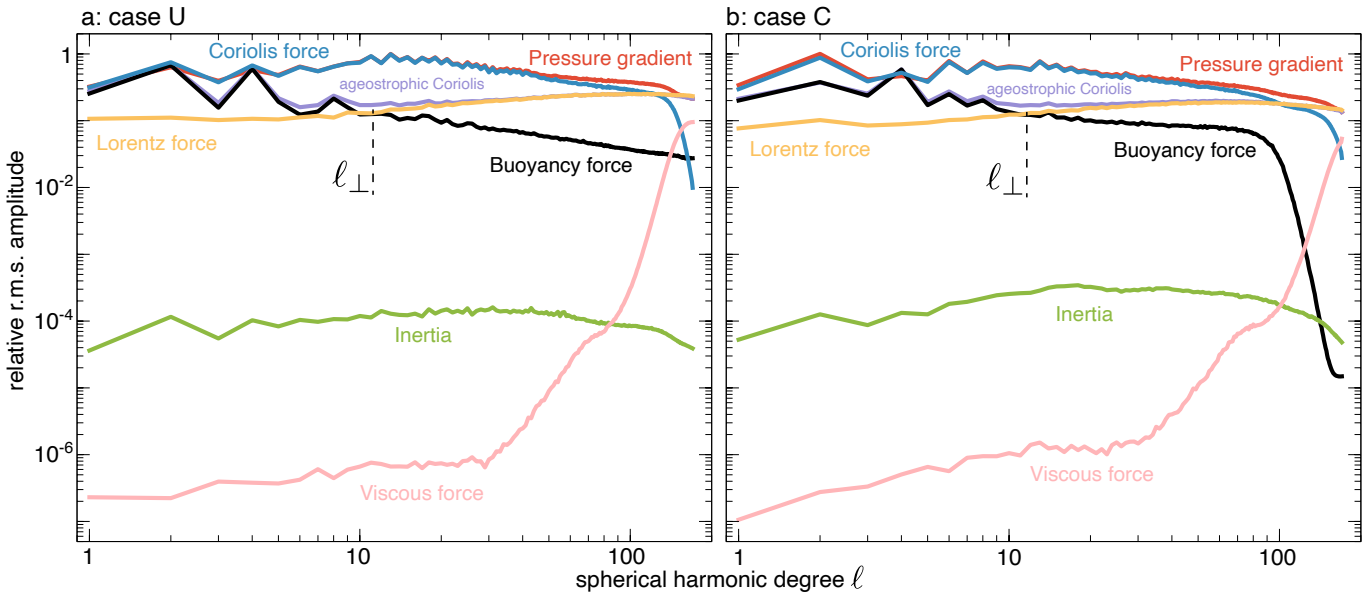

Figure 1: Root-mean-squared amplitudes of the forces in a snapshot of case U (a) and case C (b), represented as functions of the spherical harmonic degree ℓ. Force are normalised respectively to the peak of the Coriolis force.

3 Results

We first examine in Fig. 1 the length-scale dependent force balance in cases U and C. Consistently with earlier results (Aubert and Gillet, 2021), the leading-order balance is a quasi-geostrophic (QG) equilibrium between pressure and Coriolis forces. At the next order, a MAC balance is observed between the part of the Coriolis force not balanced by the pressure gradient (termed ageostrophic Coriolis force), the buoyancy force (at large scales $\ell < \ell_\perp$) and the Lorentz force (at smaller scales $\ell > \ell_\perp$). Because case U uses enhanced thermochemical diffusivity across all scales, the tail of the buoyancy force line (Fig. 1a) does not feature the steep decay seen for case C (Fig. 1b) which uses a smaller base diffusivity and small-scale hyperdiffusion (Tab. 1). The force balance structure is otherwise essentially unchanged, underlining the robustness of its behaviour against this change of modelling strategy.

It has been demonstrated that when the dynamo is in this QG-MAC force balance, the degree $\ell_\perp$ at which the buoyancy and Lorentz forces intersect determines its characteristic length scale (Schwaiger et al., 2021), because this is the point where the former works against the latter to build up the magnetic energy. Here we find $\ell_\perp = 11$ in both cases U and C, corresponding to a scale $d_\perp = \pi D/\ell_\perp \approx D/4$, a value remarkably similar to most other cases previously computed along and across the parameter space paths leading to core conditions (Aubert et al., 2017; Aubert and Gillet, 2021; Schwaiger et al., 2021; Aubert, 2023), regardless of whether hyperdiffusivity is used or not in the simulation (Aubert, 2019). Following the discussion of section 2.3, the reason why this value is so weakly variable across such a wide range of conditions is that it is unconstrained by the solenoidal force balance. The system therefore adopts the largest possible scale given the morphological constraints that there must be at least a convective up/downwelling in order to draw energy from convection, and that the fluid flow needs to avoid regions of high magnetic pressure where most of the dynamo energy is stored. The typical dynamo length scale remains about the same throughout the parameter space simply because these two constraints also remain the same.

At the following order, inertia comes about three orders of magnitude below the previous forces. Schwaiger et al. (2019) have shown that the ratio between the Lorentz and inertial force is accurately represented by the magnetic to kinetic energy ratio $B^2/\rho\mu U^2 = (\tau_U/\tau_A)^2 \approx 3-4\times10^3$ (see the Supplementary Spreadsheet). This indicates that the slow evolution of the dynamo, governed by the MAC balance on the overturn time scale $\tau_U \approx 110$ yr and longer is essentially inertialess (Aubert, 2020) and that rapid magneto-inertial wave dynamics can set up at the time scale $\tau_A \approx 2$ yr (Tab. 1) with low dissipation (Aubert and Gillet, 2021), as attested by the value $S = \tau_\eta/\tau_A > 6\times10^4$ of the Lundquist number. Finally, the viscous force is last in the hierarchy and essentially irrelevant, being found 7 orders of magnitude below the MAC forces at large scales $\ell \leq 30$, and not perturbing the leading-order balance at small scales despite the use of hyperdiffusion.

In Fig. 2 we examine the evolution of dimensionless model outputs along the parameter space paths defined in section 2.2 and explored in our previous studies (Aubert et al., 2017; Aubert and Gillet, 2021), now that we are able to complete them with new cases at their ends, and particularly with case C following the original set-up. The outputs adhere to theoretical scalings based on the QG-MAC balance, the energy budget and the closure hypothesis that $d_\perp$ is invariant along the path (Aubert et al., 2017): $Ro \sim \epsilon^{1/2}$, $\lambda/f_{\rm ohm}^{1/2} \sim \epsilon^{1/4}$, $A \sim \epsilon^{1/4}$ (Fig. 2a-c). End-of-path values are also very close to the Earth's core estimates (Aubert et al., 2017). The ohmic fraction reaches $f_{\rm ohm} = 0.91$ for case C at the end of the path (Fig. 2d), demonstrating that despite the use of hyperdiffusivity, power is essentially dissipated through ohmic losses. Cases U and N logically reach lower final $f_{\rm ohm}$ values because they operate with lower magnetic diffusivity. Consistently with the hypothesis underlying the definition of the path (Aubert et al., 2017), the magnetic dissipation length scale $d_{\rm min}$ is nearly constant (Fig. 2e) if the magnetic Reynolds number Rm is kept constant, e.g. with $Rm \approx 1000$ for all previously computed cases as well as case C. Cases U and N op-

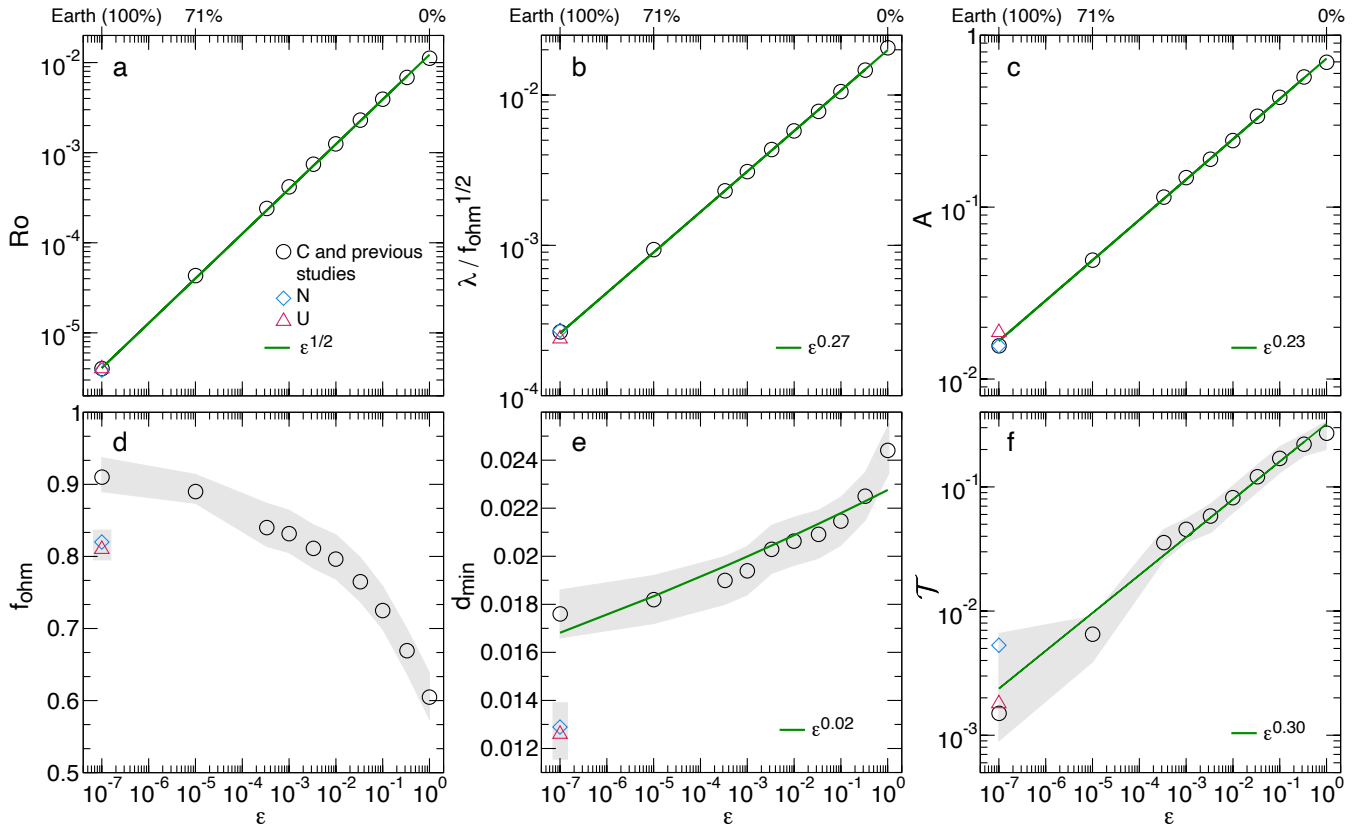

Figure 2: Evolution of the main dimensionless model outputs with the path parameter ϵ. Shown with circles are the fully resolved solution at the start of path ($\epsilon = 1$), the hyperdiffusive solutions along the path previously obtained in Aubert et al. (2017); Aubert and Gillet (2021), together with the results from cases C (circles), N (diamonds), U (triangles) now reported at $\epsilon = 10^{-7}$ (100% of the path, Earth's core conditions). Shaded grey areas represent the ±1 standard deviations, where applicable. Green lines are power-law least-squares fits, with the exponent reported in each subfigure. In (e) the least-squares fit is restricted to the cases operating at the same magnetic Reynolds number $Rm \approx 1000$ (i.e. case C and the cases from previous studies, circles).

erate at about twice this value and logically feature smaller dissipation length scales consistent with a $Rm^{-1/2}$ scaling (Christensen and Tilgner, 2004). The level of Taylor constraint enforcement $\mathcal{T} \approx 2 - 5 \times 10^{-3}$ reached at the end of path (Fig. 2f) is consistent with the extrapolations originally made in Aubert et al. (2017) and with the gap observed in Fig. 1 between inertia and the Lorentz force.

Fig. 3 presents visualisations of the velocity, density anomaly and magnetic fields within the fluid shell for case U. We find typical root-mean-squared amplitudes $U \approx 20$ km.yr^{-1}, $B \approx 4$ mT and $C \approx 10^{-4}$ kg.m^{-3} (Fig. 3a-c) that compare favourably with classical estimates for Earth's core (see references in Tab. 1). It should be stressed that different from previous studies that approached the core conditions without reaching them (e.g. Aubert and Gillet, 2021), this is directly the output of the model, and not the result of an extrapolation to these conditions using the path scaling rules. The large-scale, dipole-dominated surface magnetic field morphology (Fig. 3e) is compliant with historical observations (see χ^2 ratings in Tab. 1), and its root-mean-squared amplitude is about a tenth of the value at depth (Fig. 3c). The characteristic length scale $d_\perp \approx D/4$ of the system manifests in the longitudinal spacing between ascending or descending plumes visible in Fig. 3a,b. Downwellings are particularly prominent here because the top of the core is convectively unstable in case U. Aside from this small-scale organisation, the system features polar vortices (Fig. 3d) as well as a longitudinally hemispheric large-scale structure previously referred to as an eccentric axial 'gyre' that is also seen in Earth's core (e.g. Finlay et al., 2023). The fluid is ascending at the eastern end of the gyre and descending at the western end (Fig. 3b), and features a westward surface circulation at low latitudes in between (shaded region of Fig. 3d). The velocity and magnetic field structures drift westwards at a speed of about 0.1°.yr^{-1} comparable to geomagnetic observations (Finlay and Jackson, 2003), under the influence of the solid-body rotation resulting from the outer core-mantle-inner core rotational coupling (Aubert et al., 2013). Similar structures have been obtained in this last study through heterogeneous boundary forcing, whereas Schaeffer et al. (2017) and the present case U feature an eccentric gyre with spatially homogeneous boundaries. This longitudinally hemispheric structure can indeed be rendered convectively unstable in presence of an ambient axial magnetic field (e.g. Sakuraba, 2002). Finally, wave-like motion of rapid (interannual to interdecadal) periods and rapid westward propagation (a few degrees per year) is visible at low latitudes (Fig. 3d), similar to the findings of Gillet et al. (2022); Gillet et al. (2024).

The temporal variations of the model are also in excellent agreement with those of the geodynamo, as attested by time scales for magnetic variation $\tau_{\mathrm{SV}}(\ell)$ and acceleration $\tau_{\mathrm{SA}}(\ell)$ (Fig. 4). As shown in Aubert (2023), matching the observed and simulated curves for $\tau_{\mathrm{SV}}(\ell)$ directly constrains the convective power level at which the model should operate, and this is how the power $P \approx 3$ TW of the present cases was

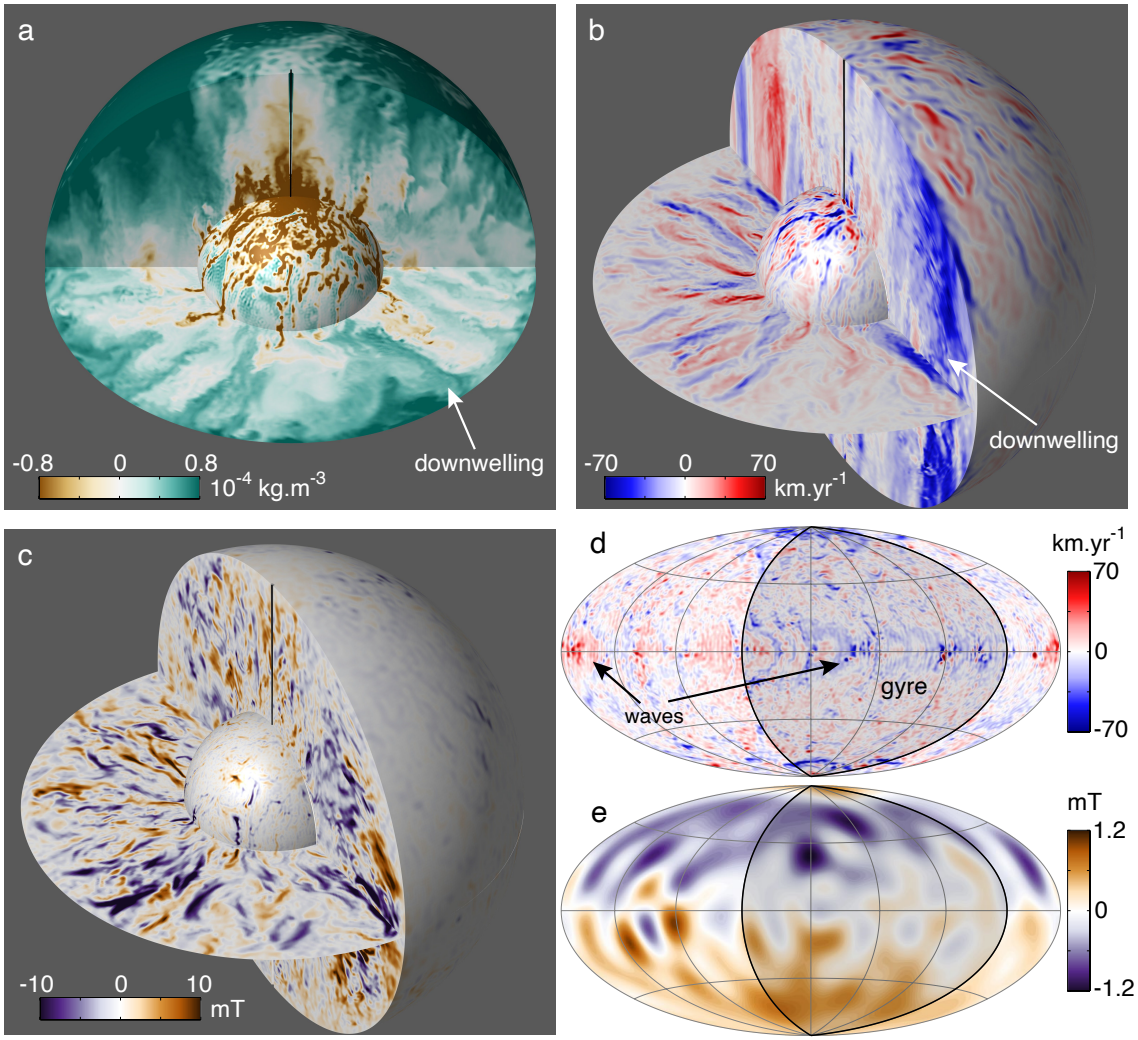

Figure 3: Representations of a snapshot taken from case U. (a) Density anomaly field C, (b) velocity $\mathbf{u}\cdot\mathbf{e}_s$ in the cylindrical axial direction, and (c) radial magnetic field $\mathbf{B}\cdot\mathbf{e}_r$, in the equatorial plane, a meridional plane, the core surface and a spherical surface at radius $r = 1.007r_i$ i.e. slightly above the inner core boundary. (d,e) Hammer projections of the core surface azimuthal velocity $\mathbf{u}\cdot\mathbf{e}_\varphi$, presented at native model resolution, and radial magnetic field presented up to spherical harmonic degree $\ell = 13$. The shaded regions in (d,e) correspond to the part of the equatorial plane that is hidden in (b,c). Note that the meridional plane represented in (a) is rotated eastwards relatively to (b,c).

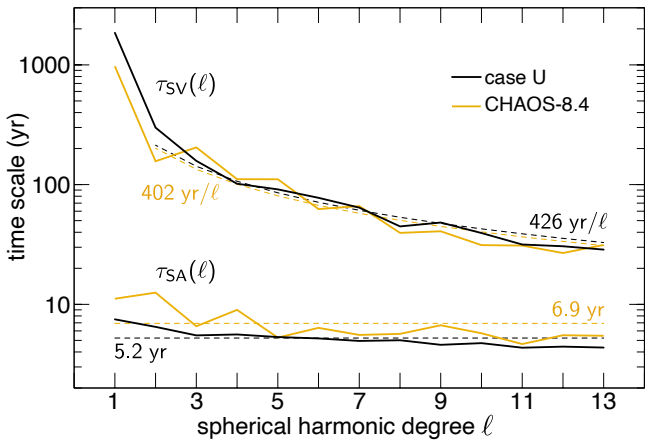

Figure 4: Magnetic variation and acceleration time scales $\tau_{SV}(\ell)$ and $\tau_{SA}(\ell)$, presented as functions of the spherical harmonic degree ℓ, for case U and the geomagnetic field model CHAOS-8.4 (Kloss et al., 2026) between 1997 and 2025.5. Least-squares fits of the results with the functional forms τ^1_{SV}/ℓ and a constant τ^0_{SA} are also reported.

selected, consistently also with the geodynamic constraints summarised in section 2.4. We note that the overall shapes of $\tau_{SV}(\ell)$, $\tau_{SA}(\ell)$ as well as the master constants $\tau^1_{SV} \approx 400$ yr, $\tau^0_{SA} \approx 6$ yr (Fig. 4, Tab. 1) are in better agreement here than they were in Aubert (2023), despite the use of data assimilation in this latter study. Earth's core conditions were indeed reached over short periods of time where the system could not equilibrate completely. In contrast, with a millennium simulated in physical time, case U is now better equilibrated from the standpoint of convective secular variations.

In Fig. 5 we further compare the temporal contents of core surface flow and magnetic accelerations between cases U0% and the 1690-yr concatenation of cases U and G (noted U+G), which are respectively located at the start (0%) and end (100%) of the same parameter space path (see section 2.2). Despite the vastly different conditions of these models, the frequency-domain power spectral densities are overlapping at the secular overturn time scale τ_U and beyond. This confirms that start-of-path models are suitable for giving an appropriate description of the system dynamics at long time scales, and that the path scaling rules used to extrapolate their output to core conditions (Aubert et al., 2017) are ac-

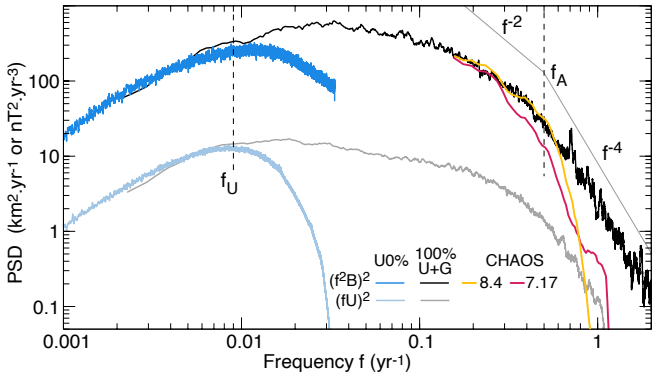

Figure 5: Frequency-domain spectral density of the total magnetic field acceleration energy $\ddot{\mathbf{B}}^2$ at Earth's surface (top) and large-scale (degree $\ell \leq 30$) flow acceleration energy $\dot{\mathbf{u}}^2$ at the core surface (bottom). Shown are the concatenation U+G of cases U and G, the case U0% at the start of the parameter space path terminating with case U, as well as the CHAOS-7.17 geomagnetic field model (Finlay et al., 2020) between 1997 and 2024, and the CHAOS-8.4 model (Kloss et al., 2026) between 1997 and 2025.5. The output of case U0% is extrapolated from the start of path towards Earth's core conditions using the path scaling rules, following the procedure in Aubert (2023). Spectral transforms are estimated with a Thomson multitaper method of half concentration bandwidth $4/\Delta t$ where $\Delta t = 1690$ yr for U+G, $\Delta t = 491400$ yr for U0%, and $\Delta t = 27$ yr, 28.5 yr for CHAOS 7.17 and CHAOS-8.4, respectively. The overturn and Alfvén frequencies $f_U = 1/\tau_U, f_A = 1/\tau_A$ are reported as well as tentative spectral falloff slopes.

curate. This also gives confidence in return that case U+G is equilibrated with respect to the longer-term dynamics. In contrast, case U+G features vastly larger power levels than case U0% in the interannual to secular time scale range. This is first because the start of path case U0% features a planetary rotation period of $2\pi/\Omega = 8.7$ yr i.e. $\sqrt{107}$ longer than Earth's (following the path scaling rules). Rotational dominance is therefore not or weakly enforced in this time scale range, whereas all time scales in case U+G are strongly rotationally-dominated since they are much longer than $2\pi/\Omega = 1$ day. Second, the large ratio between Lorentz and inertial force (Fig. 1) in case U+G enables magneto-inertial hydromagnetic waves of high quality factor at the fundamental time scale $\tau_A \approx 2$ yr (Tab. 1). As described in Aubert and Gillet (2021), this additional energy forms plateaus in the spectra of Fig. 5. The start of high-frequency fall-off for the plateaus has been related to magnetic dissipation and predicted to occur near 0.1 yr^{-1} at core conditions, a value broadly confirmed by the results of case U+G. Similarly to observations made in Aubert (2023); Aubert (2025), there appears to exist a transition in the falloff steepness near the Alfvén frequency $f_A = 1/\tau_A$, with the higher-frequency falloff then following f^{-4}. This last value is however somewhat less steep than the f^{-6} falloff observed in Aubert (2023), and we again attribute this discrepancy to short integration times in that study. The corner seen at frequency f_A presumably indicates that hydromagnetic waves are predominantly excited at large scales in the simulation. In most of the investigated frequency range, the parallelism between spectra for velocity and magnetic field underlines that magnetic acceleration predominantly results from the advection of a quasi-steady magnetic field by an accelerating flow, as classically observed at the low spherical harmonic degrees that dominate the Earth surface signal (Christensen et al., 2012; Aubert, 2018). Finally, the power density predicted by case U+G at interannual frequencies agrees with that observed in the CHAOS series of geomagnetic field models (Finlay et al., 2020; Kloss et al., 2026). The steeper high-frequency falloff of the CHAOS models is presumably due to the effects of the temporal regularisation and source separation hypotheses. Note that the CHAOS-8 series refine this temporal regularistion by using prior information derived from the end-of-path numerical dynamo sequences of Aubert (2023). This explains the enhanced high-frequency content of CHAOS-8 respectively to CHAOS-7, as well as its increased proximity with case U+G.

Inside the core, disruptions of the QG-MAC balance (Fig. 1) lead to a magneto-inertial Alfvén wave response at interannual periods commensurate with $\tau_A \approx 2$ yr (Aubert and Finlay, 2019; Gillet et al., 2022). Only axisymmetric (torsional Alfvén) waves remain of magneto-inertial nature as they ascend to the core surface, because they are immune to the Coriolis force, but these constitute a minor part of the interannual flow energy seen in Fig. 5. The main part comes from non-axisymmetric components, which are converted into quasi-geostrophic, magneto-Coriolis (QGMC) waves with similar periods during their ascent, because the influence of the Coriolis force becomes more potent than that of inertia (Gerick et al., 2021; Finlay et al., 2023; Barrois and Aubert, 2024). The QGMC wave patterns can be seen directly in the low-latitude flow at the core surface (Fig. 3d) but their typical wedge-shaped structure is more readily exhibited when highpass-filtering this flow in time and lowpass-filtering in space (Fig. 6a-c). They feature a westward phase propagation (Fig. 6d-f) at speeds of a few degrees per year that exceed by far the convective westward drift. The patterns, amplitudes and phase velocity characteristics of the waves observed in Fig. 6 are in agreement with the inferences made by Gillet et al. (2022) from rapid geomagnetic variations. Fig. 6d-f furthermore shows that the patterns of these waves are strongly variable across cases U, N, and C. Comparing cases N and C (Fig. 6e,f) first highlights the effect of a twofold decrease of the core conductivity σ, which results in patterns of significantly larger scales because of enhanced ohmic losses (see Fig. 6g). Comparing cases N and U highlights the effect of switching from a convectively neutral ($f_i = 1$) to an unstable top core ($f_i = 0.75$), which appears to force the waves at smaller scales because of the effects of enhanced convection. Note also the boundary-driven geographical segregation present in case C (Fig. 6f), where there is a preference for the Eastern hemisphere where forcing of the waves by convective upwellings is strongest.

The most notable feature of the interannual geomagnetic signals observed by geomagnetic satellites over the last 30 years is rapid recurrence of short pulses and large changes of magnetic acceleration, giving rise to geomagnetic jerk events (Chulliat et al., 2010; Finlay et al., 2020). A previous simulation that approached Earth's core conditions at 71% of the parameter space path (Aubert et al., 2022) was successful at linking these signals with the propagation of the interannual QGMC waves seen in Fig. 6. This simulation was however unable to account for the rapid recurrence of strong jerks. Fig. 7a shows that case U features frequent jerks of energy exceeding $E_J = 100\ \mathrm{nT}^2.\mathrm{yr}^{-4}$, as is the case for the satellite geomagnetic record (Fig. 7c). The recurrence time between these strong events is now about 3 years (Fig. 7b) i.e. fully

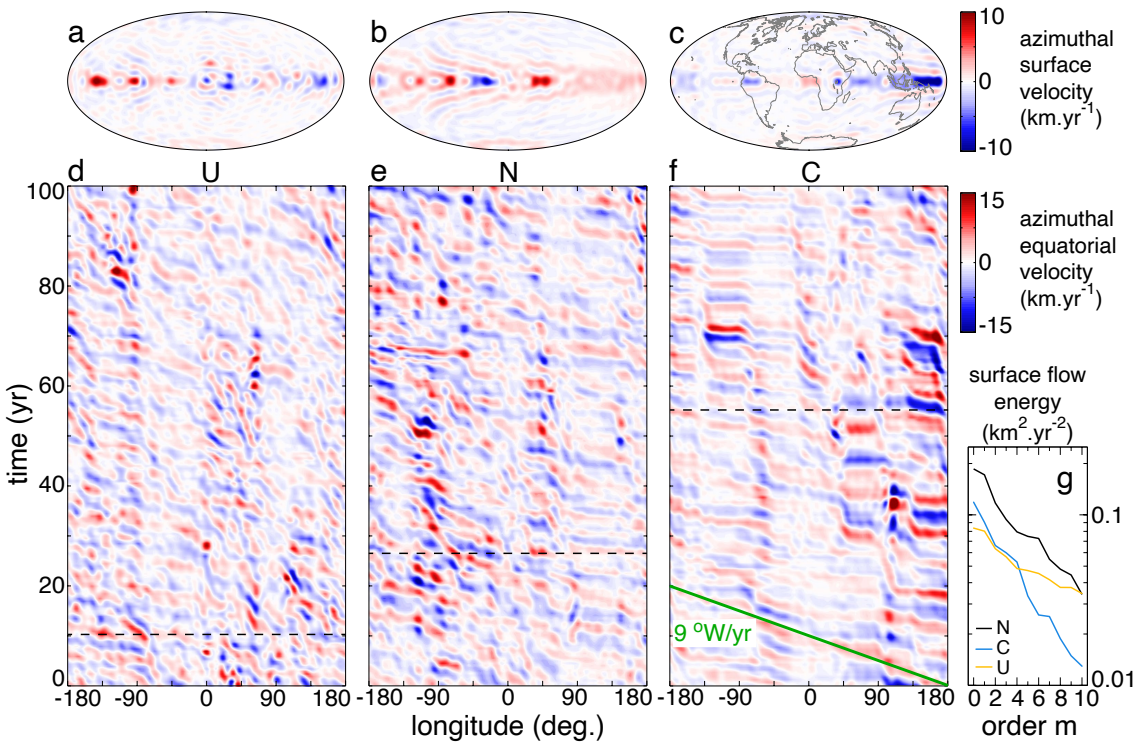

Figure 6: Azimuthal flow $\mathbf{u}\cdot\mathbf{e}_z$ at the core surface, highpass-filtered below 10 yr and truncated after spherical harmonic degree $\ell = 30$, in Hammer projections (a-c), and time-longitude plots at the equator (d-f), for cases U (a,d), N (b,e), and C (d,f). The dashed horizontal lines in (d-f) mark the instants of the snapshots (a-c). Coastlines are reported in (c) because case C has heterogeneous boundary forcing (section 2.1) while U and N have no reference longitude. A westward drift at a rate of $9^o.\mathrm{yr}^{-1}$ is indicated for reference in (c). (g) Energy spectrum of the highpass-filtered core surface flow, as a function of the spherical harmonic order m.

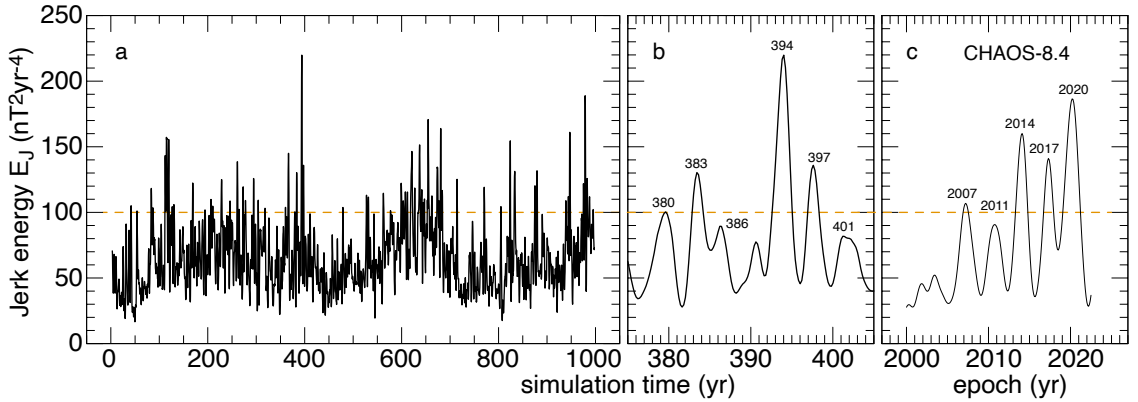

Figure 7: Jerk energy as a function of time in the entire case U (a) and in a close-up (b). (c) Jerk energy in the CHAOS-8.4 geomagnetic field model (Kloss et al., 2026). The horizontal dashed line marks the level $E_\mathrm{J} = 100\ \mathrm{nT}^2.\mathrm{yr}^{-4}$ that defines the occurrence of a jerk in Aubert et al. (2022). To facilitate the comparison, the time spans of (b) and (c) are the same.

comparable to the geomagnetic record (Fig. 7c) and as short as allowed by the averaging time window that defines E_J in connection with the limited resolution of geomagnetic acceleration models. Because the Lundquist number $S \approx 10^5$ is about 4 times larger in case U than it was in the '71% of path' model used in Aubert et al. (2022), convective excitations give rise to longer-lasting QGMC wave sequences, with more alternations giving rise to more connected jerks. Case U also more clearly illustrates the interplay between waves and the convective source, which modulates the jerk energy baseline on a secular time scale (Fig. 7a). In the light of this model, it may besides be suggested that the geodynamo is currently in a rather active convective phase. We recall that for the observed and modelled signals of Fig. 7 to agree, it is crucial that the top of the core should be neutrally buoyant (as in cases N and C) or convectively unstable (as in case U), and that stable top core stratification is strongly deleterious to this agreement (Aubert, 2025).

We now analyse the torsional magneto-inertial Alfvén waves borne by the axisymmetric azimuthal velocity. These are an important topic for simulations at core conditions, because their characteristic Alfvén time scale τ_A is interannual and realistic for the first time (Tab. 1). Fig. 8 presents time-cylindrical radius visualisations of these waves in cases GL, G and GC. The results are in morphological and quantitative agreement with geomagnetic inferences (e.g. Gillet et al., 2010; Istas et al., 2023), with amplitudes of a few tenths of a $\mathrm{km.yr}^{-1}$ (i.e. much less than QGMC waves, Fig. 6) and

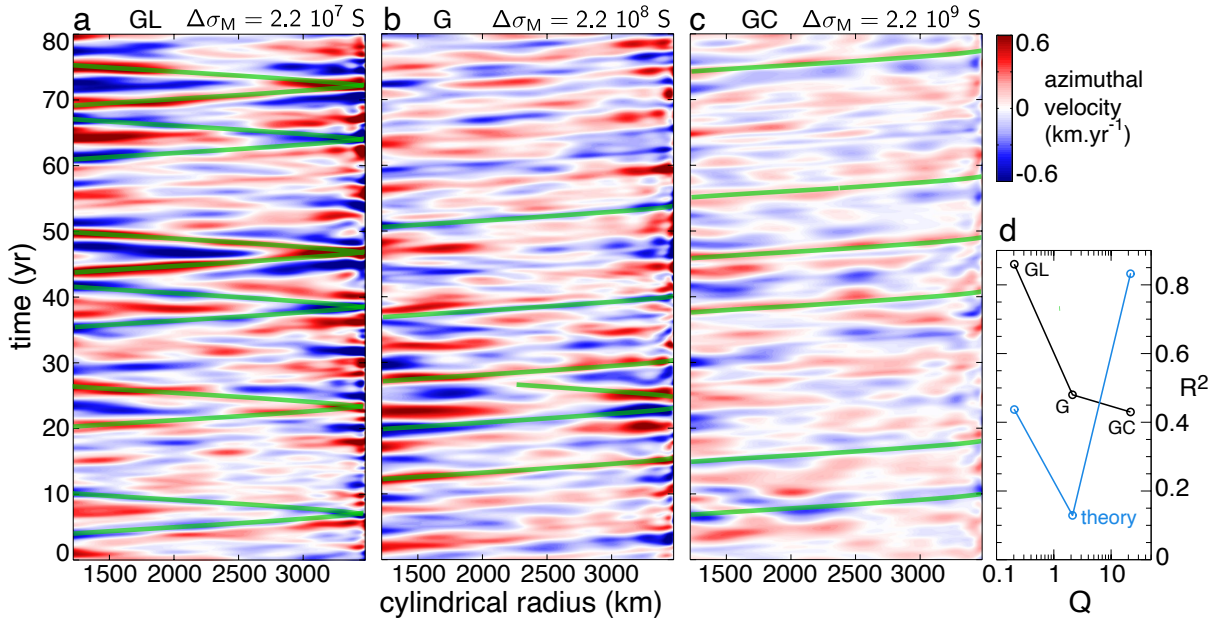

Figure 8: (a-c) Time-cylindrical radius diagrams of the axisymmetric and equator-symmetric part of the core surface azimuthal flow $\mathbf{u}\cdot\mathbf{e}_\varphi$, highpass-filtered below 10 yr and truncated after spherical harmonic degree $\ell = 30$, in (a) case GL, (b) case G, (c) case GC, which differ by their lower mantle conductance $\Delta\sigma_M$. Green curves correspond to outwards and inwards ray-tracing trajectories of waves at the Alfvén speed $c_A(s,t)$ given by eq. (11). (d) squared reflexion coefficient R^2 estimated by Radon-transforming the complete time-cylindrical radius series, as a function of the reflection quality factor Q (eq. 10). A theoretical prediction $R^2 = ((1-Q)/(1+Q))^2$ (Schaeffer and Jault, 2016; Gillet et al., 2017) is also reported.

patterns mostly reflecting the propagation of the fundamental mode at period $T_0 = \sqrt{3} r_o \tau_A / D \approx 5$ yr. Torsional waves are essentially insensitive to the outer core conductivity σ (Aubert and Gillet, 2021) but their reflection properties are sensitive to the conductance of the deep mantle $\Delta\sigma_M$ (Schaeffer and Jault, 2016). Cases GL and GC vary this property by a factor 10 on either side of the value $\Delta\sigma_M = 2.2\times10^8$ S used in case G. We find that the amplitude of torsional waves decreases with increasing $\Delta\sigma_M$ (Fig. 8a-c), in disagreement with one-dimensional modelling of the torsional wave propagation equation (Gillet et al., 2017). There appears to exist an energy cost for the core flow when strongly coupling to the mantle. This effect is not accounted for when using a fixed outer boundary and therefore infinite inertia of the mantle, as in Gillet et al. (2017). Comparing Fig. 8a-c also shows that torsional waves reflect more easily when the mantle conductance is low. This is confirmed by a Radon transform-based estimate of the reflection coefficient (Fig. 8d). This is obtained by summing the squares of the field values at different slopes in the time-cylindrical radius plot of Fig. 8a-c, identifying the two peaks corresponding to outgoing and incoming torsional waves, and computing the ratio of these two peaks. At low values of the quality factor Q, the results are at least in qualitative agreement with the theory of Schaeffer and Jault (2016) (we do not expect quantitative agreement because of the limited ability of Radon transform methods to identify the reflected energy). Clear disagreement with the theory is however observed for the highest conductance and Q value. Here again, the theoretical framework does not handle the energetic cost of moving a mantle that is more tightly coupled. If this were the case, we should indeed also expect less reflected energy at high Q values because of this cost. The geomagnetic inference does advocate for weak or no reflection (Istas et al., 2023), meaning that the conductance should probably be larger than $\Delta\sigma_M = 10^8$ S.

The millennial time series now available with case U provides a more reliable description of the interdecadal time scale range than earlier models. Fig. 9 shows that there is coherent energy in the 30-80 yr band for both cases U (Fig. 9a-c) and its start-of-path equivalent U0% (Fig. 9d-f), consistently with the power spectral densities shown in Fig. 5. This energy however has however different physical origins in the two cases. Case U0% (Fig. 9d) features eastward-drifting Rossby waves (see e.g. Aubert and Gillet, 2021) that are not geophysically realistic because of the unrealistic and nearby value of the planetary rotation rate $2\pi/\Omega = 8.7$ yr. In contrast, in case U the strong rotational and magnetic forces make QGMC waves also possible in this interdecadal range, like they were in the interannual range, provided there is an excitation source at the correct period (Barrois and Aubert, 2025) that is readily provided by convection. A stronger flow is indeed observed (compare Fig. 9a and d), comprising the landmarks of QGMC waves as they were previously observed in the interannual range (Fig. 6): westward-drifting (Fig. 9a), converging wedge patterns (Fig. 9b,c), with maximal energy at the equator. Westward drift rates at about $0.6^o.\text{yr}^{-1}$ are still significantly in excess of the convective westward drift, confirming the wave character of the flow imaged in Fig. 9a-c.

Looking for a magnetic signature of these interdecadal QGMC waves, we note that the parallelism between fU and f^2B in fig. 5 implies that $B/U \sim 1/f$ i.e. the magnetic to kinetic energy ratio of the waves increases with decreasing frequency. Whereas it has been necessary to investigate the magnetic acceleration in order to find a signature for the interannual waves (e.g. Aubert et al., 2022), for interdecadal waves a signature can be anticipated directly in the magnetic variation. Because they are not axisymmetric,

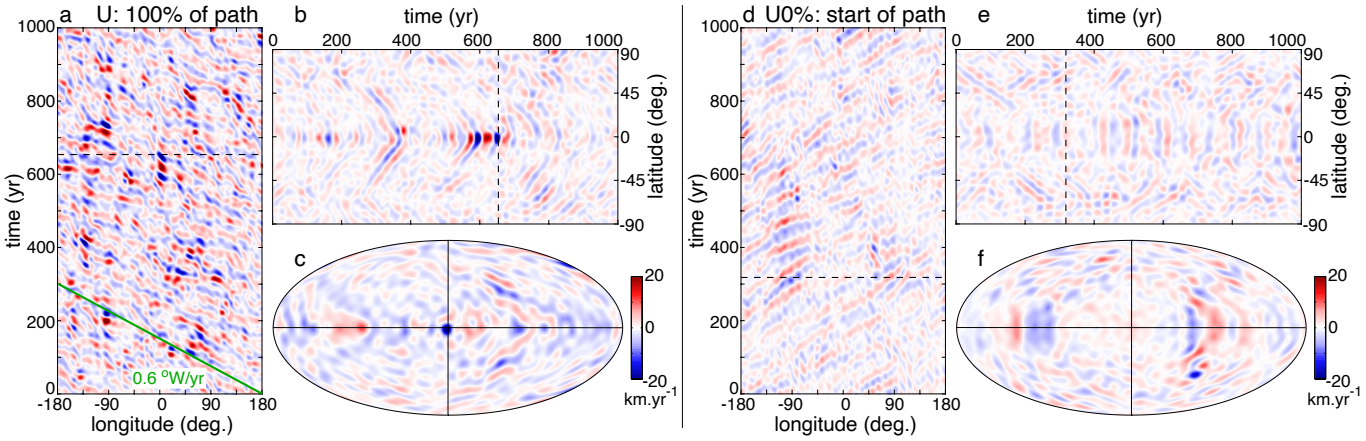

Figure 9: (a,d) Time-longitude diagram at the equator, (b,e) time-latitude diagram at a reference longitude, and (c,f) snapshot Hammer projections of the azimuthal velocity $\mathbf{u}\cdot\mathbf{e}_\varphi$, bandpass-filtered between 30 and 80-yr periods and truncated after spherical harmonic degree $\ell = 30$, in case U operating at Earth's core conditions (a,b,c) and (d,e,f) case U0% at the start of the parameter space path terminating with case U. The vertical lines in (c,f) locates the reference longitude for (b,e), and the dashed horizontal lines in (a,d) locate the time of the snapshots (c,f). A westward drift at a rate of $0.6^o.\mathrm{yr}^{-1}$ is indicated for reference in (a).

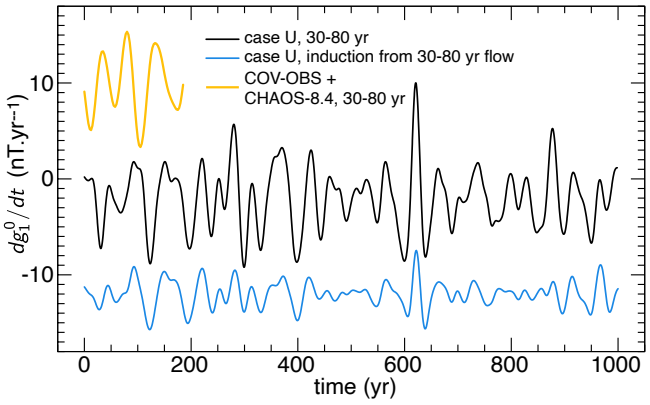

Figure 10: Time-derivative of the geomagnetic axial dipole Gauss coefficient g_1^0 (see Alken et al., 2021, for a definition), bandpass-filtered between 30 and 80-yr periods. Shown are: the dipole variations of case U (black), the part due to induction by the meridional flow u_θ bandpass-filtered between 30 and 80-yr periods, computed using eq. (12) (blue), and (orange) the concatenation of geomagnetic field model COV-OBS (Gillet et al., 2013) and CHAOS-8.4 (Kloss et al., 2026). Time series are vertically shifted for clarity.

the waves imaged in Fig. 9a-c also have a meridional component $u_\theta = \mathbf{u}\cdot\mathbf{e}_\theta$, which transports the radial magnetic field $B_r = \mathbf{B}\cdot\mathbf{e}_r$ and produces changes in the axial dipole Gauss coefficient g_1^0 through (e.g. Olson and Amit, 2006; Aubert et al., 2025)

$$\frac{\mathrm{d}g_1^0}{\mathrm{d}t} = -\int_0^\pi \frac{3r_o^2}{4r_\mathrm{E}^3}\overline{u_\theta B_r}\sin^2\theta\, d\theta. \qquad (12)$$

In Fig. 10 we use eq. (12) to confirm that a sizeable part of dipole variations at interdecadal periods indeed comes from induction by the interdecadal wave flows. Oscillations with period near 60 years furthermore have an amplitude in line with that observed in the geomagnetic dipole variations over the past 185 years. As was the case for interannual waves (Fig. 6), we recall that stable stratification at the top of the core is also strongly deleterious to this dipole variation signal (Aubert, 2025) because it is deleterious to QGMC waves.

Reaching the physical conditions of Earth's core is also important for the study of core-originated length-of-day (LOD) variations, because only then is the ratio between core, mantle, inner core inertia and the magnetic forces correct (since it relates to the Alfvén time τ_A), as well as the frequency content and amplitude of torques, angular momentum exchanges, and LOD signals. Cases U and G feature typical LOD variations of a few milliseconds over a century, similar to the observations (Fig. 11a). Torques on the order of a few times 10^{18} N.m are involved, in line with previous estimates (Holme, 1998). On time average, the mantle is driven by the gravitational torque (i.e. entrained by the inner core differentially rotating eastwards at a rate $\Omega_\mathrm{IC} - \Omega_\mathrm{M} \approx 0.1^o.\mathrm{yr}^{-1}$) and braked by the magnetic torque (i.e. dragged by the core surface westward drfit), consistently with the rotational dynamics described in Pichon et al. (2016). Introducing viscous relaxation of the inner core and a lag time of $\tau_\mathrm{IC} = 20$ yr in the gravitational torque between mantle and inner core (the difference between cases U and G) logically suppresses variations shorter than τ_IC in this torque (Fig. 11c), leaving all these rapid variations to be accounted for by the magnetic torque. Increasing the lower mantle conductance in this latter case then also logically increases this magnetic torque, and the rapid LOD variations as well (Fig. 11b). However, whereas a simple scaling of the torque at constant forcing would imply a linear increase of the LOD with mantle conductance (e.g. Pichon et al., 2016; Gillet et al., 2017), the increase observed here is clearly much less steep than linear, because the amplitude of the forcing torsional waves decreases as the mantle conductance increases (Fig. 8). Only case GC with the largest conductance $\Delta\sigma_\mathrm{M} = 2.2\times10^9$ S approximately matches the amplitude of the observed rapid LOD variations at periods between 4.5 and 7.5 yr in the vicinity of the fundamental torsional wave period $T_0 \approx 5$ yr (Fig. 11b). This is in broad agreement with the result of Gillet et al. (2015), who proposed $\Delta\sigma_\mathrm{M} = 3\times10^9$ S from the analysis of inferred core flows in this frequency band. The lower mantle conductivity case GL is inefficient at transferring the angular momentum in the interannual period range (Fig. 11b) but strikingly very efficient at dramatically increasing the angular momentum exchanges and LOD variations at interdecadal time scales (Fig. 11a,d), an effect that is further investigated in Fig. 12. The absence of such large swings

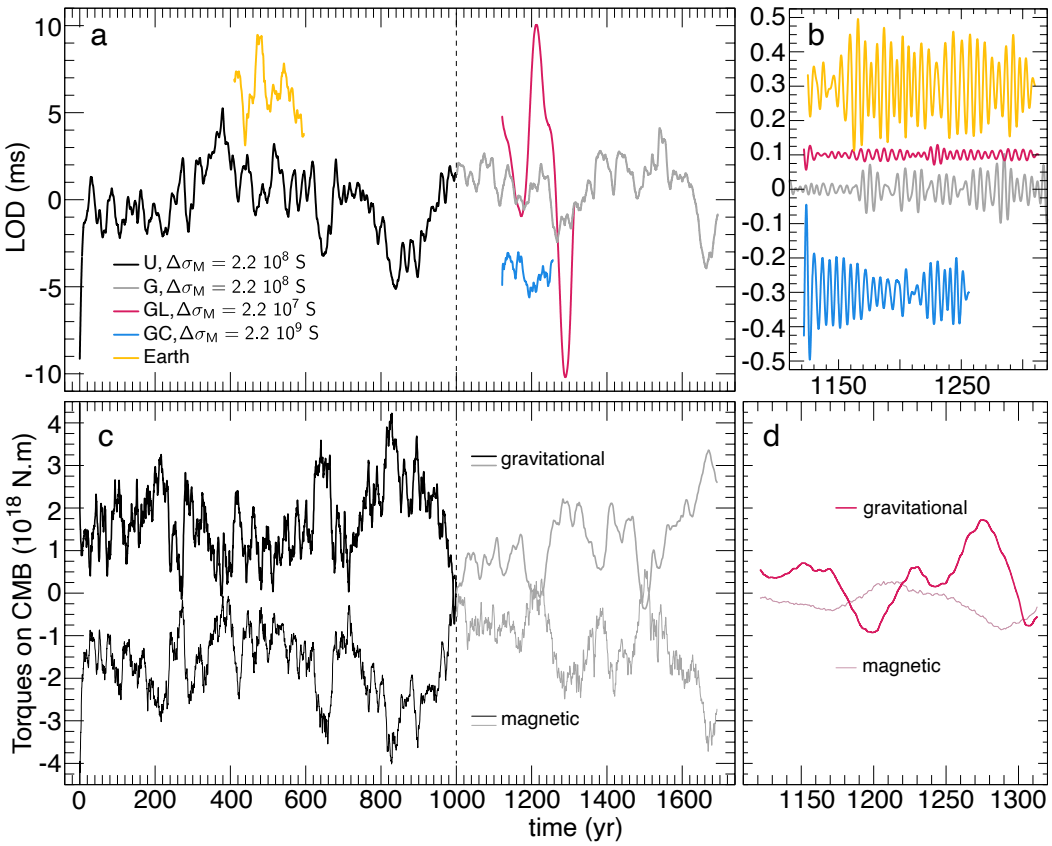

Figure 11: (a) Length-of-day (LOD) variations in cases U, G, GL and GC, together with the core-originated LOD of Earth for 1840-2025. The Earth LOD time series is the concatenation of LUNAR97 (Gross, 2001) and the IERS C04 series (Bizouard and Gambis, 2009), detrended by 1.78 ms/cy, cleaned for the atmospheric angular momentum and solid tides, and lowpass-filtered at 2 yr (processing from Rosat and Gillet, 2023). (b) LOD variations in cases G, GL, GC and Earth, bandpass-filtered between 4.5 and 7.5 yr. Time series in (a,b) are vertically shifted for clarity (Earth data is also horizontally shifted). (c) time series of the magnetic and gravitational torques $\Gamma_{M,M}$ and $-\Gamma_G$ felt by the mantle, in the cases U and G. The dashed line marks the transition between from the end of U to the beginning of G. (d) same torques for case GL.

in the observed LOD signal (Fig. 11a) again suggests that low mantle conductance values $\Delta\sigma_M \ll 10^8$ S should be discarded. More generally, this also suggests that if there indeed exists a decadal lag in the gravitational torque, then some other core-mantle coupling mechanism needs to exist and efficiently transfer the angular momentum at time scales shorter than the lag.

Further insight can be gained by examining LOD power spectral densities in Fig. 12. These are compensated for a f^{-4} falloff with frequency f, consistent with $(\mathrm{dLOD}/\mathrm{d}t)^2 \sim (\mathrm{d}\Omega_M/\mathrm{d}t)^2 \sim u^2$ from electromagnetic core-mantle coupling (e.g. Pichon et al., 2016), and the squared velocity $u^2 \sim f^{-2}$ for interannual torsional waves previously reported by Aubert and Gillet (2021). Consistent with this falloff, the plateaus found in the compensated spectra of cases G and GC between periods 3 and 20 years confirm that LOD variations in this range are due to angular momentum exchanges with torsional waves in the outer core fluid. Consistently with Fig. 11 also, the interannual LOD variations increase with lower mantle conductance, and our highest simulated value of mantle conductance $\Delta\sigma_M = 2.2\times10^9$ S (case GC) is needed to approach the Earth LOD frequency content. It is difficult to single out a systematic and outstanding peak at the fundamental period $T_0 \approx 5$ yr of torsional waves. Likewise, the period $2\pi\sqrt{I_{IC}I_M/\Gamma(I_{IC}+I_M)} = 6.3$ yr of the mantle-inner core gravitational coupling mode does not stand out, as expected in a context where the torsional wave fundamental

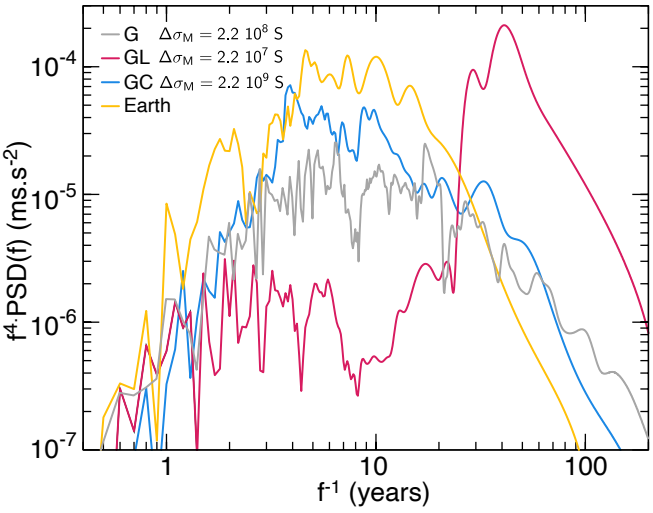

Figure 12: Power spectral density of the length-of-day series from cases G, GC, GL and from Earth data, compensated by f^4, as functions of the period $1/f$. Earth data is obtained as in Fig. 11 but limited to its most precise part 1962-2025. Spectral transforms are estimated with a Thomson multitaper method of half concentration bandwidth $4/\Delta t$ where $\Delta t = t_{run}$ for the simulations and $\Delta t = 63$ yr for the Earth series.

period T_0 is as short as the period of this mode (Dumberry, 2025). However, parts of the outer core axial fluid cylinders

can be magnetically locked in co-rotation with the inner core, such that the actual period of this mantle-'outer core' gravitational coupling mode should be longer (Dumberry, 2025). This situation appears especially relevant to the lower mantle conductance case GL. In this case indeed, the mantle is coupled to the outer core only indirectly, via the gravitational torque followed by the magnetic torque at the inner core boundary, such that the mantle sees the inner core as well as a part of the outer core as a unique, gravitationally coupled, body. Assuming that the outer core is coupled up to cylindrical radius $s \geq r_i$, the period to consider then becomes $T(s) = 2\pi\sqrt{I_{\rm OC}(s) I_{\rm M}/\Gamma(I_{\rm OC}(s) + I_{\rm M})}$, where

$$I_{\rm OC}(s) = \frac{4}{15}\pi\rho r_o^5 \left[2 - (1-(s/r_o)^2)^{3/2}(3(s/r_o)^2+2)\right] \quad (13)$$

is the moment of inertia of the core between cylindrical radii 0 and s. Matching $T(s)$ to the resonant periods in excess of 40 yr observed in Fig. 12 for case GL requires $s \geq 0.6 r_o$ i.e. that the core is coupled over more than 60% of its cylindrical radius at these periods. The period corresponding to an entirely coupled core is $T(r_o) = 81$ yr, in line with the few oscillations observed for case GL in Fig. 11a. Notably, we observe that the coupling extends over considerably more than the axial cylinder tangent to the inner core ($s = r_i = 0.35 r_o$), probably because of the large-scale nature of the torsional waves that maintain this coupling on time scales shorter than $T(s)$.

4 Discussion

4.1 Success of the convective geodynamo paradigm

In the simulations presented here, and for the first time without extrapolation, all model outputs and particularly $U \approx 20$ km.yr.$^{-1}$, $B \approx 4$ mT, $C \approx 10^{-4}$ kg/m^3 match the Earth estimates strikingly well (Tab. 1). The morphology of the surface magnetic field, the flow structures (Fig. 3), as well as their variations and accelerations (Fig. 4) are quantitatively Earth-like, and feature the notable structures previously described in the literature (see the review of Finlay et al., 2023): the slow convective westward drift, the longitudinally hemispherical gyre (Fig. 3), interdecadal dipole variations (Fig. 10), rapid interannual QGMC waves with faster westward propagation (Fig. 6), the associated jerk events (Fig. 7), torsional waves (Fig. 8) and their associated core-originated variations in the length of the day (Figs 11 and 12). In particular, it is key to obtain an Alfvén time $\tau_A \approx 2$ yr that is Earth-like for the first time, in order to explain most of the wave-driven features occurring at interannual time scales, as well as core-mantle angular momentum exchanges. It is also key that the simulation duration matches or exceeds the magnetic variation time scale $\tau_{\rm SV}^1 \approx 400$ yr, in order to ascertain that it is well equilibrated from the standpoint of long-term convective variations.

Having reached the end of the parameter space path defined in Aubert et al. (2017) over about 17 overturn times of the core therefore provides a direct validation of the convective geodynamo paradigm. From the sole specification of first-principle physics and a few fundamental parameters (length, density, rotation rate, power, electrical conductivity), we are now in position to reproduce the behaviour of the geodynamo with excellent accuracy. The strategy to enhance small-scale viscosity while keeping it much lower than the magnetic diffusivity at large scales pays off, as the viscous force is essentially irrelevant here (Fig. 1) because its contribution to energy dissipation is minor (Fig. 2). Ideally, the computation should carry on for at least a decay time of the dipole (about 50 kyr), to make sure that dynamo action is fully demonstrated and the statistics well equilibrated. However, it should be recalled that the simulation results from a gradual approach of Earth's core conditions along parameter space paths, where dynamo action, outputs and scalings have been checked at various intermediate positions (Fig. 2 and Aubert et al., 2017; Aubert, 2019; Aubert and Gillet, 2021). If the dynamo should have failed, or behaved differently from the scaling predictions, this should therefore have occurred much earlier along these paths. The robustness of long-term induction mechanisms is also strenghtened by the similarity between start-of-path extrapolations and end-of-path realisations at time scales beyond the core overturn (Fig. 5).

Because of this long-term invariance, too, a probable outstanding discrepancy with the geodynamo is that none of the models presented here would present dipole reversals if they could be integrated over millions of years and longer, because none of the previous models have featured reversals either (Aubert et al., 2017). The difficulty is that classical reversal mechanisms based on the inertia-driven multipolar transition become inefficient once the magnetic to kinetic energy ratio $B^2/\rho\mu U^2 = (\tau_U/\tau_A)^2$ increases (Tassin et al., 2021). Very few reversing dynamos with low inertia have been exhibited so far in the standard set-up (Jones and Tsang, 2025), and whether their mechanism can be extrapolated to Earth is currently unclear. An inertialess reversal mechanism valid at core conditions has been presented (Aubert et al., 2025), but this requires a stable top core incompatible with rapid geomagnetic variations (Aubert, 2025), and has therefore not been implemented here. Further work is needed, searching for similarly robust mechanisms that would also hold in neutral or superadiabatic top core conditions.

Here we have successfully tested a modification of the path approach where we have enhanced the thermochemical diffusivity κ at all spatial scales, instead of ramping up its value at small scales with a hyperdiffusivity profile, as was originally done in Aubert et al. (2017). In terms of dimensionless numbers, this means that the Prandtl number $Pr = \nu/\kappa$ decreases along the path, to reach values of order 10^{-3} at its end, instead of being kept equal to unity. The path theory does indeed not specify a particular rule for this parameter. We have observed that the force balance, as well as the system dynamics, are unchanged by this modification (Fig. 1). Because the Péclet number $Pe = UD/\kappa \geq 1000$ remains sufficiently high, the system indeed stays in an advection-dominated regime where the details of density anomaly diffusion do not influence the dynamics and the energy route from injection to dissipation. The numerical computation is also facilitated as we can reliably use a smaller radial resolution NR in the radial direction (Tab. 1) when using this modification.

4.2 Geodynamic implications

Given its accuracy, the model can be considered a reliable and first-principle based physical link between geomagnetic and

geodetic observables of the core on one hand, and the underlying deep Earth geodynamic parameters on the other hand. A power (or ohmic dissipation) level near $P = 3$ TW is needed to quantitatively match these observables, in agreement with a more systematic previous determination (Aubert, 2023). We note that this power level in turn requires fairly high values of the core-mantle boundary heat flow (e.g. Labrosse, 2015), consistent with the recent multi-disciplinary estimate $Q_{\mathrm{CMB}} \approx 15$ TW (Frost et al., 2022, see section 2.4). It could in principle become possible to distinguish between a neutrally buoyant and a convectively unstable top core, or to constrain the conductivity σ of the outer core from the signature of rapid QGMC waves at the core surface (Fig. 6) but the rather low resolution of current geomagnetic inferences (Gillet et al., 2022) makes this more theoretical than practical for the time being. In any case, we recall that any geophysically plausible level of stable stratification at the top of the core is strongly deleterious to the success of the model (Aubert, 2025), such that the combination of this model and the geomagnetic evidence is strongly supportive of a top core that is at least neutrally buoyant.

In the hypothesis of direct electromagnetic coupling across the core-mantle boundary, torsional waves (Fig. 8) and their associated core-mantle angular momentum exchanges (Figs 11 and 12) are informative on the conductance of the lower mantle. The reflection, attenuation properties at the core surface, as well as the predicted variations in the length of the day support a lower mantle conductance in excess of $\Delta\sigma_{\mathrm{M}} = 10^9$ S, in agreement with the inference of Gillet et al. (2015). This is however fairly high when compared to the available determinations from electromagnetic sounding, and this would in any case require to distribute materials with a highly enriched content in iron (i.e. with conductivity σ_{M} approaching the core conductivity σ) over a layer with thickness $\Delta = O(10)$ km, sufficiently thin to avoid phase lags in magnetic variations (Gillet et al., 2025).

We have explored a configuration where the viscous relaxation time of the inner core $\tau_{\mathrm{IC}} = 20$ yr lies in the interdecadal range. The gravitational torque is then unable to account for interannual core-mantle angular momentum exchanges (Fig. 11). In this case, suppressing direct coupling across the core-mantle boundary triggers the resonance of a 'mantle-outer core gravitational mode' at interdecadal periods, with a striking but non-geophysical signature. Some form of direct coupling across the core surface is therefore needed, and if this is provided by an electromagnetic torque, the lower mantle conductance cannot be very much smaller than $\Delta\sigma_{\mathrm{M}} = O(10^8$ S).

4.3 Explaining and predicting the interdecadal geomagnetic variations

By virtue of the millennial physical time duration of the model sequences, we were able to uncover quasi-geostrophic, magneto-Coriolis waves in the interdecadal range (Fig. 9), with a signature in the dipole variation signal (Fig. 10). The apparent 60-yr periodicity of the geomagnetic dipole variation has previously motivated several explanations involving torsional (Zatman and Bloxham, 1997) or magneto-Archimedes-Coriolis waves (Buffett, 2014). The former interpretation has been abandoned with the downward re-evaluation of τ_A towards interannual values (Gillet et al., 2010), and the stable top core required by the latter is strongly incompatible with the rapid geomagnetic signal (Aubert, 2025). Here, we propose that this signal is caused by QGMC waves, the presence of which is exhibited here in a fully dynamically consistent framework, and at levels compatible with the geomagnetic signal (Fig. 10).

Because Earth's core QGMC waves have already been exhibited at periods up to 12 yr in geomagnetic inferences (Gillet et al., 2024), it will be interesting to investigate the possibility of their existence at even longer periods in forthcoming inverse problem studies that should incorporate the temporal dependence of these waves as prior information. The use of statistical priors from numerical dynamos approaching or matching Earth's core conditions has started to bear fruit in observation-based geomagnetic field and core flow modelling (Gillet et al., 2022; Istas et al., 2023; Claveau et al., 2025; Kloss et al., 2026). With robust synthetic data now acquired over several millennia, and a new understanding of interdecadal waves as well as their signatures, we hope to be able to simulate the wave dynamics over realistic magnetic base states. This could unlock geomagnetic predictions at a range of a few years with a lower Earth surface error than the typical 100 nT that is currently feasible (Fournier et al., 2021).

4.4 Refining the dynamo scaling laws

The model has confirmed the extremely robust character of the QG-MAC force balance and associated large-scale structure (Figs 1 and 3), that were previously observed along and across paths in parameter space (Aubert et al., 2017; Schwaiger et al., 2019). Because the path parameter is a dimensionless measure of convective power, the following scaling laws based on the convective power P could also be validated:

$$U = (P/\rho\Omega D^3)^{1/2}, \tag{14a}$$

$$B = 0.1\sqrt{\rho\mu}(P\Omega/\rho D)^{1/4}, \tag{14b}$$

where prefactors have been determined from Fig. 2. These can be derived from the MAC balance and the power budget with the additional closure assumption that $d_\perp$ remains constant (Starchenko and Jones, 2002; Aubert et al., 2017). We have indeed found (Fig. 1) that at core conditions, the system organises at a scale $d_\perp = \pi D/\ell_\perp \approx D/4$ that has varied little (at most a factor 2) along the parameter space path (Aubert et al., 2017), but also across this path as long as the dynamo remains in QG-MAC balance (Schwaiger et al., 2021), and regardless of whether hyperdiffusion is used or not (Aubert, 2019). We stress that the solenoidal force balance alone does not constrain $d_\perp$, such that the full force balance including gradients (as computed in Fig. 1) is needed to access it. Another argument in favour of these laws is the excellent accuracy with which they can simultaneously predict the estimates $U \approx 5\times10^{-4}$ m.s^{-1} and $B \approx 4$ mT for Earth's core with a single and plausible estimate of the convective power $P = 3$ TW, once their prefactors are determined from the numerical simulations (Figs 2 and 3, Tab. 1).

In contrast, the classical dynamo scaling laws (Davidson, 2013) close the system of equations by assuming the independence of B on the rotation rate, which leads to a variable dynamo length scale $d_\perp$. The widely known resulting scaling

$B \sim P^{1/3}$ has received strong numerical support in the numerically moderate part of the parameter space (Christensen and Aubert, 2006), where structural constraints from the magnetic field remain weak and viscous dissipation is not necessarily minor. Significant discrepancies have however appeared since more advanced simulations have become available. The associated $d_\perp \sim P^{1/9}$ scaling for length scale predicts a factor $(10^7)^{1/9} \approx 6$ decrease between moderate and Earth's core conditions, which has not materialised, as stated above. Being able to vary the power over such a wide range also provides sufficient accuracy to discriminate between the $U \sim P^{4/9}$ of this theory and $U \sim P^{1/2}$ from Eq. (14a), in favour of the latter (Aubert, 2019). Finally, when calibrated from the numerical simulations, the predictions from these laws have remained slightly inconsistent with Earth data. Aubert et al. (2009) for instance obtain $U \approx 2\times10^{-3}$ m.s^{-1} and $B \approx 2.5$ mT for $P \approx 3$ TW. At first glance the difference is not very large between these and the above predictions, and acceptable, coming from a scaling theory. But because B lies slightly below and U significantly above the Earth estimates of Tab. 1, the discrepancies cannot be resolved by varying the power P, whereas there is a plausible value of P for which both scalings (14a,14b) pinpoint the Earth estimates.

Despite these inconsistencies, it remains true that the $P^{1/3}$ scaling has been successful at explaining magnetic field amplitudes varying over three orders of magnitudes between planets and fully convective stars (Christensen et al., 2009). But we note that the dynamic of a $P^{1/4}$ scaling would only differ by a factor two over this range. This could be accommodated by the uncertainties involved in observing and estimating the internal magnetic fields, thus bringing us back to the initial proposal of Starchenko and Jones (2002). The results presented here certainly incite to continue the search for a universal scaling theory, because of the importance of the associated laws for comparative planetology.

Acknowledgements

JA thanks two anonymous referees for reviews and comments on the manuscript. This project has been funded by ESA in the framework of EO Science for Society, through contract 4000148713/25/NL/FFi (SWARM + 4D Earth Core+). Numerical computations were performed at S-CAPAD, IPGP and using HPC resources from GENCI-TGCC and GENCI-CINES (Grant numbers A0180402122 and A0200402122). The results presented in this work rely on data collected at magnetic observatories. The national institutes that support them and INTERMAGNET are thanked for promoting high standards of magnetic observatory practice (www.intermagnet.org).

Data availability

The Supplementary Spreadsheet, simulation data and codes supporting this study can be found at doi:10.18715/IPGP.2026.mm0sx2m0, and from the corresponding author upon request.

Competing interests

The author declares no competing interests.

References

Ahrens, T. J. (1995). Global Earth Physics: A Handbook of Physical Constants. Vol. 1. Washington, DC: AGU. DOI: 10.1029/RF001.

Alken, P. et al. (2021). International Geomagnetic Reference Field: the thirteenth generation. *Earth Planets Space* 73.1, 49. DOI: 10.1186/s40623-020-01288-x.

Aubert, J., C. C. Finlay, and A. Fournier (2013). Bottom-up control of geomagnetic secular variation by the Earth's inner core. *Nature* 502, 219–223. DOI: 10.1038/nature12574.

Aubert, J. (2018). Geomagnetic acceleration and rapid hydromagnetic wave dynamics in advanced numerical simulations of the geodynamo. *Geophys. J. Int.* 214.1, 531–547. DOI: 10.1093/gji/ggy161.

Aubert, J. (2019). Approaching Earth's core conditions in high-resolution geodynamo simulations. *Geophys. J. Int.* 219.S1, S137–S151. DOI: 10.1093/gji/ggz232.

Aubert, J. (2020). Recent geomagnetic variations and the force balance in Earth's core. *Geophys. J. Int.* 221.1, 378–393. DOI: 10.1093/gji/ggaa007.

Aubert, J. (2023). State and evolution of the geodynamo from numerical models reaching the physical conditions of Earth's core. *Geophys. J. Int.* 235.1, 468–487. DOI: 10.1093/gji/ggad229.

Aubert, J. (2025). Rapid geomagnetic variations and stable stratification at the top of Earth's core. *Phys. Earth. Planet. Int.* 362, 107335. DOI: 10.1016/j.pepi.2025.107335.

Aubert, J. and C. C. Finlay (2019). Geomagnetic jerks and rapid hydromagnetic waves focusing at Earth's core surface. *Nature Geosci.* 12.5, 393–398. DOI: 10.1038/s41561-019-0355-1.

Aubert, J., T. Gastine, and A. Fournier (2017). Spherical convective dynamos in the rapidly rotating asymptotic regime. *J. Fluid. Mech.* 813, 558–593. DOI: 10.1017/jfm.2016.789.

Aubert, J. and N. Gillet (2021). The interplay of fast waves and slow convection in geodynamo simulations nearing Earth's core conditions. *Geophys. J. Int.* 225, 1854–1873. DOI: 10.1093/gji/ggab054.

Aubert, J., S. Labrosse, and C. Poitou (2009). Modelling the palaeo-evolution of the geodynamo. English. *Geophys. J. Int.* 179.3, 1414–1428. DOI: 10.1111/j.1365-246X.2009.04361.x.

Aubert, J., M. Landeau, A. Fournier, and T. Gastine (2025). Core-surface kinematic control of polarity reversals in advanced geodynamo simulations. *Phys. Earth Planet. Int.* 364, 107365. DOI: j.pepi.2025.107365.

Aubert, J., P. W. Livermore, C. C. Finlay, A. Fournier, and N. Gillet (2022). A taxonomy of simulated geomagnetic jerks. *Geophys. J. Int.* 231.1, 650–672. DOI: 10.1093/gji/ggac212.

Aurnou, J., M. Calkins, J. Cheng, K. Julien, E. King, D. Nieves, K. Soderlund, and S. Stellmach (2015). Rotating convective turbulence in Earth and planetary cores. *Phys. Earth. Planet. Int.* 246, 52–71. DOI: 10.1016/j.pepi.2015.07.001.

Barrois, O. and J. Aubert (2024). Characterization of hydromagnetic waves propagating over a steady, non-axisymmetric background magnetic field. *Proc. Roy. Soc. A* 480.2300, 20240067. DOI: 10.1098/rspa.2024.0067.

Barrois, O. and J. Aubert (2025). Influence of background magnetic fields on the excitation of Magneto-Coriolis

modes inside the Earth's core. *J. Stud. Earth Deep Inter.* 1, 3. DOI: 10.46298/jsedi.15652.

Berrada, M. and R. A. Secco (2021). Review of Electrical Resistivity Measurements and Calculations of Fe and Fe-Alloys Relating to Planetary Cores. *Frontiers Earth Sci.* Volume 9 - 2021. DOI: 10.3389/feart.2021.732289.

Bizouard, C. and D. Gambis (2009). The Combined Solution C04 for Earth Orientation Parameters Consistent with International Terrestrial Reference Frame 2005. *Geodetic Reference Frames: IAG Symposium Munich, Germany, 9-14 October 2006*. Ed. by H. Drewes. Berlin, Heidelberg: Springer Berlin Heidelberg, pp. 265–270. DOI: 10.1007/978-3-642-00860-3_41.

Buffett, B. A. (2014). Geomagnetic fluctuations reveal stable stratification at the top of the Earth's core. *Nature* 507.7493, 484–487. DOI: 10.1038/nature13122.

Buffett, B. (1996). A mechanism for decade fluctuations in the length of day. English. *Geophys. Res. Lett.* 23.25, 3803–3806. DOI: 10.1029/96GL03571.

Buffett, B. (1997). Geodynamic estimates of the viscosity of the Earth's inner core. English. *Nature* 388.6642, 571–573. DOI: 10.1038/41534.

Christensen, U. and A. Tilgner (2004). Power requirement of the geodynamo from ohmic losses in numerical and laboratory dynamos. *Nature* 429, 169–171. DOI: 10.1038/nature02508.

Christensen, U. R., J. Aubert, F. H. Busse, P. Cardin, E. Dormy, S. Gibbons, G. A. Glatzmaier, Y. Honkura, C. A. Jones, M. Kono, M. Matsushima, A. Sakuraba, F. Takahashi, A. Tilgner, J. Wicht, and K. Zhang (2001). A numerical dynamo benchmark. *Phys. Earth Planet. Int.* 128, 25–34. DOI: 10.1016/S0031-9201(01)00275-8.

Christensen, U. R., J. Aubert, and G. Hulot (2010). Conditions for Earth-like geodynamo models. English. *Earth. Plan. Sci. Let.* 296.3-4, 487–496. DOI: 10.1016/j.epsl.2010.06.009.

Christensen, U. R., V. Holzwarth, and A. Reiners (2009). Energy flux determines magnetic field strength of planets and stars. *Nature* 457.7226, 167–169. DOI: 10.1038/nature07626.

Christensen, U. R., I. Wardinski, and V. Lesur (2012). Timescales of geomagnetic secular acceleration in satellite field models and geodynamo models. *Geophys. J. Int.* 190.1, 243–254. DOI: 10.1111/j.1365-246X.2012.05508.x.

Christensen, U. R. and J. Aubert (2006). Scaling properties of convection-driven dynamos in rotating spherical shells and application to planetary magnetic fields. *Geophys. J. Int.* 166, 97–114. DOI: 10.1111/j.1365-246X.2006.03009.x.

Chulliat, A., E. Thebault, and G. Hulot (2010). Core field acceleration pulse as a common cause of the 2003 and 2007 geomagnetic jerks. *Geophys. Res. Lett.* 37. DOI: 10.1029/2009GL042019.

Claveau, R., N. Gillet, P.-O. Amblard, and C. C. Finlay (2025). Broadband a priori temporal cross-covariances for the geomagnetic inverse problem: application to the satellite era. *Earth Planets Space* 77.1, 126. DOI: 10.1186/s40623-025-02248-z.

Davidson, P. A. (2013). Scaling laws for planetary dynamos. *Geophys. J. Int.* 195.1, 67–74. DOI: 10.1093/gji/ggt167.

Davies, C., M. Pozzo, D. Gubbins, and D. Alfè (2015). Constraints from material properties on the dynamics and evolution of Earth's core. *Nature Geosci.* 8.9, 678–685. DOI: 10.1038/ngeo2492.

Davies, C. J., D. R. Stegman, and M. Dumberry (2014). The strength of gravitational core-mantle coupling. *Geophys. Res. Lett.* 41.11, 3786–3792. DOI: 10.1002/2014GL059836.

de Wijs, G., G. Kresse, L. Vocadlo, D. Dobson, D. Alfe, M. Gillan, and G. Price (1998). The viscosity of liquid iron at the physical conditions of the Earth's core. *Nature* 392.6678, 805–807. DOI: 10.1038/33905.

Dumberry, M. (2025). The mantle-inner core gravitational mode of oscillation in a strong magnetic field regime. *J. Stud. Earth Deep Inter.* 1, 1. DOI: 10.46298/jsedi.15735.

Finlay, C. C., N. Gillet, J. Aubert, P. W. Livermore, and D. Jault (2023). Gyres, jets and waves in the Earth's core. *Nature Reviews Earth & Environ.* 4.6, 377–392. DOI: 10.1038/s43017-023-00425-w.

Finlay, C. C. and A. Jackson (2003). Equatorially dominated magnetic field change at the surface of Earth's core. *Science* 300, 2084–2086. DOI: 10.1126/science.1083324.

Finlay, C. C., C. Kloss, N. Olsen, M. D. Hammer, L. Tøffner-Clausen, A. Grayver, and A. Kuvshinov (2020). The CHAOS-7 geomagnetic field model and observed changes in the South Atlantic Anomaly. *Earth Planets Space* 72.1, 156. DOI: 10.1186/s40623-020-01252-9.

Fournier, A., J. Aubert, V. Lesur, and E. Thébault (2021). Physics-based secular variation candidate models for the IGRF. *Earth, Planets, Space* 73.1, 190. DOI: 10.1186/s40623-021-01507-z.

Frost, D. A., M. S. Avery, B. A. Buffett, B. A. Chidester, J. Deng, S. M. Dorfman, Z. Li, L. Liu, M. Lv, and J. F. Martin (2022). Multidisciplinary Constraints on the Thermal-Chemical Boundary Between Earth's Core and Mantle. *Geochem. Geophys. Geosyst.* 23.3, e2021GC009764. DOI: 10.1029/2021GC009764.

Gerick, F., D. Jault, and J. Noir (2021). Fast Quasi-Geostrophic Magneto-Coriolis Modes in the Earth's Core. *Geophys. Res. Lett.* 48.4, e2020GL090803. DOI: 10.1029/2020GL090803.

Gillet, N., D. Jault, and E. Canet (2017). Excitation of travelling torsional normal modes in an Earth's core model. *Geophys. J. Int.* 210.3, 1503–1516. DOI: 10.1093/gji/ggx237.

Gillet, N., D. Jault, E. Canet, and A. Fournier (2010). Fast torsional waves and strong magnetic field within the Earth's core. *Nature* 465.7294, 74–77. DOI: 10.1038/nature09010.

Gillet, N., D. Jault, and C. C. Finlay (2015). Planetary gyre, time-dependent eddies, torsional waves and equatorial jets at the Earth's core surface. *J. Geophys. Res.* 120, 3991–4013. DOI: 10.1002/2014JB011786s.

Gillet, N., D. Jault, C. C. Finlay, and N. Olsen (2013). Stochastic modeling of the Earth's magnetic field: Inversion for covariances over the observatory era. *Geochem. Geophys. Geosyst.* 14.4, 766–786. DOI: 10.1002/ggge.20041.

Gillet, N., F. Dall'Asta, P.-o. Amblard, R. Claveau, and J. Aubert (2024). Waves in Earth's core and geomagnetic field forecast. *Phys. Earth Planet. Int.* 357, 107284. DOI: 10.1016/j.pepi.2024.107284.

Gillet, N., F. Gerick, D. Jault, T. Schwaiger, J. Aubert, and M. Istas (2022). Satellite magnetic data reveal interannual waves in Earth's core. *Proc. Natl. Acad. Sci. U.S.A.* 119.13, e2115258119. DOI: 10.1073/pnas.2115258119.

Gillet, N., Z. Martinec, T. Lepage, and D. Jault (2025). Constraints on the lower mantle electrical conductivity from length-of-day changes. *J. Stud. Earth Deep Inter.* 1, 4. DOI: 10.46298/jsedi.16005.

Glatzmaier, G. and P. Roberts (1995). A 3-dimensional self-consistent computer simulation of a geomagnetic field reversal. *Nature* 377.6546, 203–209. DOI: 10.1038/377203a0.

Glatzmaier, G. A. (2002). Geodynamo Simulations—How Realistic Are They? *Ann. Rev. Earth. Plan. Sci.* 30, 237–257. DOI: 10.1146/annurev.earth.30.091201.140817.

Gomi, H., K. Ohta, K. Hirose, S. Labrosse, R. Caracas, M. J. Verstraete, and J. W. Hernlund (2013). The high conductivity of iron and thermal evolution of the Earth's core. *Phys. Earth Planet. Int.* 224, 88–103. DOI: 10.1016/j.pepi.2013.07.010.

Gross, R. S. (2001). A combined length-of-day series spanning 1832-1997: LUNAR97. *Phys. Earth Planet. Int.* 123.1, 65–76. DOI: 10.1016/S0031-9201(00)00217-X.

Gubbins, D. (2001). The Rayleigh number for convection in the Earth's core. *Phys. Earth. Planet. Int.* 128.1, 3–12. DOI: 10.1016/S0031-9201(01)00273-4.

Holme, R. (1998). Electromagnetic core-mantle coupling - I. Explaining decadal changes in the length of day. *Geophys. J. Int.* 132, 167–180. DOI: 10.1046/j.1365-246x.1998.00424.x.

Istas, M., N. Gillet, C. C. Finlay, M. D. Hammer, and L. Huder (2023). Transient core surface dynamics from ground and satellite geomagnetic data. *Geophys. J. Int.* 233.3, 1890–1915. DOI: 10.1093/gji/ggad039.

Jones, C. A. and Y.-K. Tsang (2025). Low inertia reversing geodynamos. *Phys. Earth. Planet. Int.* 360, 107303. DOI: 10.1016/j.pepi.2024.107303.

Kageyama, A., T. Miyagoshi, and T. Sato (2008). Formation of current coils in geodynamo simulations. *Nature* 454.7208, 1106–1109. DOI: 10.1038/nature07227.

Kageyama, A., T. Sato, and the Complexity Simulation Group (1995). Computer simulation of a magnetohydrodynamic dynamo. II. *Physics of Plasmas* 2.5, 1421–1431. DOI: 10.1063/1.871485.

Kloss, C., C. C. Finlay, N. Olsen, L. Tøffner-Clausen, N. Gillet, and A. Grayver (2026). The CHAOS-8 geomagnetic field model. *Earth Planets Space* 78.1, 21. DOI: 10.1186/s40623-025-02352-0.

Kuang, W. and J. Bloxham (1997). An Earth-like numerical dynamo model. *Nature* 389.6649, 371–374. DOI: 10.1038/38712.

Kutzner, C. and U. Christensen (2002). From stable dipolar to reversing numerical dynamos. *Phys. Earth Planet. Int.* 131, 29–45. DOI: 10.1016/S0031-9201(02)00016-X.

Labrosse, S. (2015). Thermal evolution of the core with a high thermal conductivity. *Phys. Earth Planet. Int.* 247, 36–55. DOI: 10.1016/j.pepi.2015.02.002.

Le Bars, M. and D. Lemasquerier (2026). Laboratory Experiments in Geophysical and Astrophysical Fluid Dynamics. *Ann. Rev. Fluid. Mech.* 58.Volume 58, 2026, 301–329. DOI: 10.1146/annurev-fluid-112723-053838.

Lhuillier, F., A. Fournier, G. Hulot, and J. Aubert (2011). The geomagnetic secular-variation timescale in observations and numerical dynamo models. *Geophys. Res. Lett.* 38, L09306. DOI: 10.1029/2011GL047356.

Lister, J. R. (2003). Expressions for the dissipation driven by convection in the Earth's core. *Phys. Earth Planet. Int.* 140.1-3, 145–158. DOI: 10.1016/j.pepi.2003.07.007.

Menu, M. D., L. Petitdemange, and S. Galtier (2020). Magnetic effects on fields morphologies and reversals in geodynamo simulations. *Phys. Earth Planet. Int.* 307, 106542. DOI: 10.1016/j.pepi.2020.106542.

Miyagoshi, T., A. Kageyama, and T. Sato (2010). Zonal flow formation in the Earth's core. *Nature* 463.7282, 793–796. DOI: 10.1038/nature08754.

Nataf, H.-C. and N. Schaeffer (2015). Turbulence in the Core. *Treatise on Geophysics*. Elsevier BV, pp. 161–181. DOI: 10.1016/b978-0-444-53802-4.00142-1.

Nimmo, F. (2015). Energetics of the Core. *Treatise on Geophysics (Second Edition)*. Ed. by G. Schubert. Second Edition. Oxford: Elsevier, pp. 27–55. DOI: 10.1016/B978-0-444-53802-4.00139-1.

Ohta, K., H. Inoue, S. Suehiro, K. Hirose, S. Kawaguchi-Imada, and H. Dekura (2025). Electrical and thermal conductivities of Fe–Ni–Si alloy under core conditions: A reevaluation. *Phys. Earth Planet. Int.* 363, 107531. DOI: 10.1016/j.pepi.2025.107351.

Olson, P., U. Christensen, and G. A. Glatzmaier (1999). Numerical modelling of the geodynamo: mechanisms of field generation and equilibration. *J. Geophys. Res.* 104.B5, 10383–10404. DOI: 10.1029/1999JB900013.

Olson, P. and H. Amit (2006). Changes in Earth's dipole. *Naturwissenschaften* 93.11, 519–542. DOI: 10.1007/s00114-006-0138-6.

Pichon, G., J. Aubert, and A. Fournier (2016). Coupled dynamics of Earth's geomagnetic westward drift and inner core super-rotation. *Earth Planet. Sci. Lett.* 437, 114–126. DOI: 10.1016/j.epsl.2016.01.004.

Pozzo, M., C. J. Davies, D. Gubbins, and D. Alfè (2012). Thermal and electrical conductivity of iron at Earth's core conditions. *Nature* 485.7398, 355–358. DOI: 10.1038/nature11031.

Pozzo, M., C. J. Davies, and D. Alfè (2022). Towards reconciling experimental and computational determinations of Earth's core thermal conductivity. *Earth. Planet. Sci. Lett.* 584, 117466. DOI: 10.1016/j.epsl.2022.117466.

Rochester, M. G. (1962). Geomagnetic core-mantle coupling. *J. Geophys. Res.* 67.12, 4833–4836. DOI: 10.1029/JZ067i012p04833.

Rosat, S. and N. Gillet (2023). Intradecadal variations in length of day: Coherence with models of the Earth's core dynamics. *Phys. Earth Planet. Int.* 341, 107053. DOI: 10.1016/j.pepi.2023.107053.

Sakuraba, A. (2002). Linear magnetoconvection in rotating fluid spheres permeated by a uniform axial magnetic field. *Geophys. Astrophys. Fluid Dyn.* 96.4, 291–318. DOI: 10.1080/03091920290024234.

Sakuraba, A. and P. H. Roberts (2009). Generation of a strong magnetic field using uniform heat flux at the surface of the core. English. *Nature Geosci.* 2.11, 802–805. DOI: 10.1038/NGEO643.

Schaeffer, N. (2013). Efficient spherical harmonic transforms aimed at pseudospectral numerical simulations. *Geophys. Geochem. Geosystems.* 14.3, 751–758. DOI: 10.1002/ggge.20071.

Schaeffer, N., D. Jault, H.-C. Nataf, and A. Fournier (2017). Turbulent geodynamo simulations: a leap towards Earth's core. *Geophys. J. Int.* 211.1, 1–29. DOI: 10.1093/gji/ggx265.

Schaeffer, N. and D. Jault (2016). Electrical conductivity of the lowermost mantle explains absorption of core torsional waves at the equator. *Geophys. Res. Lett.* 43.10, 4922–4928. DOI: 10.1002/2016gl068301.

Schwaiger, T., T. Gastine, and J. Aubert (2019). Force balance in numerical geodynamo simulations: a systematic study. *Geophys. J. Int.* 219.S1, S101–S114. DOI: 10.1093/gji/ggz192.

Schwaiger, T., T. Gastine, and J. Aubert (2021). Relating force balances and flow length scales in geodynamo simulations. *Geophys. J. Int.* 224.3, 1890–1904. DOI: 10.1093/gji/ggaa545.

Sheyko, A., C. Finlay, J. Favre, and A. Jackson (2018). Scale separated low viscosity dynamos and dissipation within the Earth's core. *Sci. Rep.* 8.1, 12566. DOI: 10.1038/s41598-018-30864-1.

Soderlund, K. M., A. Sheyko, E. M. King, and J. M. Aurnou (2015). The competition between Lorentz and Coriolis forces in planetary dynamos. *Prog. Earth. Plan. Sci.* 2.1, 1–10. DOI: 10.1186/s40645-015-0054-5.

Starchenko, S. and C. Jones (2002). Typical Velocities and Magnetic Field Strengths in Planetary Interiors. *Icarus* 157.2, 426–435. DOI: 10.1006/icar.2002.6842.

Takahashi, F., M. Matsushima, and Y. Honkura (2005). Simulations of a quasi-Taylor state geomagnetic field including polarity reversals on the Earth Simulator. English. *Science* 309.5733, 459–461. DOI: 10.1126/science.1111831.

Tassin, T., T. Gastine, and A. Fournier (2021). Geomagnetic semblance and dipolar–multipolar transition in top-heavy double-diffusive geodynamo models. *Geophys. J. Int.* 226.3, 1897–1919. DOI: 10.1093/gji/ggab161.

Taylor, J. (1963). The magneto-hydrodynamics of a rotating fluid and the Earth's dynamo problem. English. *Proc. Roy. Soc. A* 9, 274–283. DOI: 10.1098/rspa.1963.0130.

Teed, R. J. and E. Dormy (2025). Scaling of Strong-Field Spherical Dynamos. *Geophys. Res. Lett.* 52.20. e2025GL118078 2025GL118078, e2025GL118078. DOI: 10.1029/2025GL118078.

Yadav, R. K., T. Gastine, U. R. Christensen, S. J. Wolk, and K. Poppenhaeger (2016). Approaching a realistic force balance in geodynamo simulations. *Proc. Natl. Acad. Sci. U.S.A.* 113.43, 12065–12070. DOI: 10.1073/pnas.1608998113.

Zatman, S. and J. Bloxham (1997). Torsional oscillations and the magnetic field within the Earth's Core. *Nature* 388, 760–763. DOI: 10.1038/41987.

The article *Geodynamo simulations spanning millennia in the physical conditions of Earth's core* © 2026 by Julien Aubert is licensed under CC BY 4.0.